

# 2

## The Measurement Process: MR Data Collection and Image Analysis

**Paul Tofts**

*Department of Medical Physics, NMR Research Unit, Institute of Neurology, University College London, Queen Square, London WC1N 3BG, UK*

---

2.1 MR Data Collection	17
2.2 Image Analysis, Statistics and Classification	39

---

### 2.1 MR DATA COLLECTION

The process of collecting MR data from a subject, in the form of images, spectra or maps, is analysed in some detail.

#### 2.1.1 Subject Positioning and the Pre-scan Procedure

The subject is positioned on the scanner couch by the radiographer (technologist). The subject should be comfortable, to reduce movement during the scan as much as possible. The radiographer should use their insight into the subject's emotional

state to reduce anxiety if necessary; preparation on a separate couch may be helpful. A cushion under the knees can reduce cramp. Occasionally it is desirable to place the subject prone. *Prone positioning* of the head may be more comfortable if support is provided for the forehead and cheekbones, leaving a gap for the nose, as used in a massage table. Movement of the body can cause a head movement; a nasal positioning device (Tofts *et al.*, 1990) can help cooperative subjects to keep still. Some patients will find it hard to keep still because of their disease. Study investigators are usually motivated to keep very still. Some

kinds of movement are very common, especially rotation in the sagittal plane. Movement can be monitored by repeated localizer images throughout the study. If spatial registration between different image datasets is used (see Chapter 15), then the amount of movement that took place is available as output from the program. Research on why some subjects move and on what limits how long a subject can stay in the scanner, would improve the quality of MR data that can be obtained. In the future, it may be possible to use fast imaging to dynamically alter the slice positions, tracking the movement of a subject in real time (although movement to a location of different static or RF field value would require some sophisticated correction). If Gd contrast agent is to be injected, a line may be placed into the subject's arm, so that injection can be carried out whilst retaining the original positioning of the subject. A power injector is often used to provide a consistent injection procedure, with synchronization to the scanner.

After the subject has been placed in the magnet bore, the automatic *pre-scan* procedure generally includes the following steps that take account of differences between subjects, and are crucial to quantification. The receiver gain is adjusted to use the available dynamic range of the receiver channel, without overloading it. The gain must be fixed for subsequent scans, if image intensity values are to be combined in some way (e.g. for a dynamic Gd scan, where images are collected at a range of time points after injection of contrast agent – see Chapter 10, Figure 10.2). The transmitter output is adjusted to give the desired flip angle (FA) in the subject. This can be carried out in a number of ways; ideally, only the signal from the relevant piece of tissue (e.g. a slice or a spectroscopic voxel) is optimized. A multislice acquisition cannot have the correct FA at all locations, because of transmit field nonuniformity. It may be useful to record the values of receive and transmit gain at the time of scanning (unless these are automatically stored in the image header).

The pulse sequences, containing long lists of radiofrequency (RF) and magnetic field gradient pulses, are then run. Signals are recorded; localization of the origin of the signal is achieved using

a combination of slice selection and frequency-encoding and phase-encoding gradients. Images can be  $T_1$ - or  $T_2$ -weighted (see Chapters 5 and 6). Coordinate axes used usually correspond to  $z$  in the direction of the static field  $B_0$ , so that magnetization precesses in the  $x$ - $y$  plane. Images are reconstructed using Fourier transformation; the magnitude of the complex data is usually calculated (this is not vulnerable to unpredictable phase shifts). Full descriptions of the MR imaging process are available elsewhere (Callaghan, 1993; Haacke *et al.*, 1999 and Chapter 6).

### 2.1.2 The NMR Signal

The signal  $\delta v$  from precessing nuclei in a small volume  $\delta V_s$  in the sample is given by (Hoult and Richards, 1976; Hoult, 1978):

$$\delta v = \omega_0 B_{1xy} M_{xy} \delta V_s \cos(\omega_0 t) \quad (2.1)$$

where  $\omega_0$  is the Larmor<sup>1</sup> frequency (in  $\text{rad s}^{-1}$ ).  $B_{1xy}$  is the component<sup>2</sup> of the RF field  $B_1$  produced in the transverse plane at the location of the sample by unit current in the coil, during transmission.  $M_{xy}$  is the transverse component of the magnetization of the sample.<sup>3</sup> For protons the equilibrium magnetization  $M_0$  is:<sup>4</sup>

$$M_0 = \frac{N \gamma \hbar^2 B_0}{4kT} \quad (2.2)$$

where  $N$  is the number of protons per unit volume,  $\gamma$  is the *magnetogyric ratio*,<sup>5</sup>  $\hbar = h/2\pi$ , where  $h$  is Planck's constant,  $B_0$  is the magnitude of

<sup>1</sup> The *Larmor frequency* is the frequency at which protons precess around the main static field  $B_0$ . The life of Sir Joseph Larmor, the Irish physicist, is described by Tubridy and McKinsty (2000).

<sup>2</sup> A linear coil produces two counter-rotating components; one is in the right direction for NMR and is useful; the other is not used, but contributes to noise and power requirements. In a circularly polarized coil only the useful component is produced and detected.

<sup>3</sup> After a single  $90^\circ$  RF pulse,  $M_{xy} = M_0$ .

<sup>4</sup> See also the book by Haacke *et al.* (1999), p. 86.

<sup>5</sup>  $\gamma = \omega_0/B_0$ , where  $B_0$  is the static magnetic field strength, in Tesla. For protons,  $\gamma = 2.675 \times 10^8 \text{ rad s}^{-1} \text{ T}^{-1}$  (equivalent to  $42.57 \text{ MHz T}^{-1}$ ) (Haacke *et al.*, 1999). Greek letters are defined in Appendix 1.

the main static magnetic field,  $k$  is Boltzmann's constant and  $T$  is the absolute temperature<sup>6</sup> of the sample.

The proportionality of the received signal with the magnitude of the applied  $B_1$  field per unit current, shown in Equation (2.1), is called the *principle of reciprocity* (Hoult and Richards, 1976), and is a key concept in qMR. In simple terms, it says that, if we have trouble getting the applied  $B_1$  field into a particular location in the sample using a particular coil, we will have as much trouble getting the signal out of that location using the same coil. This is discussed in more detail in Section 2.1.9 below.

The dependence of magnetization on absolute temperature is relevant when room temperature concentration standards are used (as in measurements of proton density and metabolite concentrations, see Chapters 4 and 9). As a particular concentration of protons is cooled (for example from body temperature to room temperature), its magnetization increases and it can produce more signal.

### 2.1.3 The Static Magnetic Field $B_0$

In a superconducting magnetic, the value of the static field is set at the time of installation by adjusting the amount of circulating current stored in the windings. There may be a very small decay over time, which is compensated by adjusting the current through room temperature windings, or by adjusting the centre frequency of the transmitter.

When the subject is placed in the magnet, the magnetic susceptibility of the tissue alters the field inside the brain slightly. The transmitter centre frequency is adjusted to bring the protons back onto resonance. The shim coil currents are adjusted to obtain a spatially uniform  $B_0$  distribution, as far as possible.

Remaining static field gradients caused by spatially varying tissue susceptibility (particularly near tissue–air interfaces, such as the temporal

lobes) can be a problem, particularly for spectroscopy and echo planar imaging, which are very sensitive to such gradients (see Figure 12.9, which shows a map of the magnetic field distortion throughout a typical human head). In spectroscopy the line position will be altered and possibly broadened. In gradient echo and echo planar imaging there may be signal dropout due to intra-voxel dephasing.<sup>7</sup> In spin echoes, the dephasing effect of these gradients is corrected provided the spins are stationary; however in the presence of diffusion, spins moving through a gradient will not be rephased and signal loss will once again be seen. Such signal loss will not normally cause systematic error in quantification, although the lowered signal-to-noise ratio (SNR) will give increased random errors, and in situations where the absolute signal level is important (e.g. proton density, PD) there will also be a systematic error. A further source of degradation is that echo planar images (and to a lesser extent gradient echo images, which have a shorter echo time than echo planar sequences) will suffer geometric distortion, such that the image is shifted or warped in the locality of susceptibility gradients (see for example Moerland *et al.*, 1995; Jezzard, 2002; Hutton *et al.*, 2002). This in turn prevents straightforward spatial registration of such images with those having negligible distortion (principally those that are spin-echo based), and prevents any attempt at measuring volume. The image intensity is likely to be altered by distortion (since a given amount of signal will be placed into a voxel that is too large or too small). A third degradation is that off-resonance effects in such localities may reduce the apparent FA and distort the slice profile.

The static field can be mapped straightforwardly using the phase shift after a gradient echo (see for example Sled and Pike, 2000; Skinner and Glover, 1997; Jezzard and Balaban, 1995; Willcott *et al.*, 1987).

<sup>7</sup> In *intra-voxel dephasing*, the different components of magnetization in a voxel, experiencing different static fields, become out of phase with each other, and the total transverse magnetization vector in the voxel is reduced. In a spin echo, this dephasing is corrected by the 180° refocusing pulse; in a gradient echo the uncorrected dephasing leads to signal loss.

<sup>6</sup> The *absolute temperature* is measured in degrees Kelvin (K) from  $-273^\circ\text{C}$ , which is absolute zero. Thus freezing point ( $0^\circ\text{C}$ ) is 273 K, and body temperature ( $37^\circ\text{C}$ ) is 310 K.

### 2.1.4 Static Field Gradients

Having taken a lot of care to achieve a uniform static magnetic field, switched field gradients are deliberately introduced as part of the imaging process. The slew rates are very fast, giving switching times of  $<1$  ms. Eddy currents can be induced in surrounding conducting structures; these have the effect of producing small transient shifts in  $B_0$ , distorting spectra and images. Eddy currents are reduced to low levels by several devices. Actively shielded gradient coils limit the magnetic flux outside the coil; current pre-emphasis circuits drive the coils in such a way as to counteract the effects of the eddy currents; and conduction loops are eliminated from the scanner bore.

The remaining non idealities are two-fold. Firstly, the *gradient amplitudes* may be incorrect, by up to about 1%. This gives rise to small errors in the size of objects (since the gradient change corresponds to a change in magnification, or of voxel size), and also to errors in the estimates of diffusion coefficients and tensors. Very precise measurements of voxel dimensions, using image registration, enable the value of small gradient changes to be measured (Lemieux and Barker, 1998). Secondly, gradient coils do not produce a completely linear variation of static field with distance (i.e. the gradients are nonuniform); this in turn produces errors in the gradient amplitude (according to the position), and gives rise to spatial distortion (Moerland *et al.*, 1995; Jezzard, 2002). Nonlinearity from gradient coils can be reduced by using the body gradient coils, instead of the head coils, although the switching time may be compromised. Some manufacturers measure and correct for the geometric distortion caused by nonlinearity, either in two dimensions (i.e. just within the slice<sup>8</sup>) or with a complete three-dimensional solution.

### 2.1.5 Radiofrequency Transmit Field $B_1$

Typical pulse amplitudes are 10–20  $\mu\text{T}$ . Sometimes amplitudes are expressed in Hz or  $\text{rad s}^{-1}$ ,

<sup>8</sup> The ‘gradwarp’ scheme on General Electric machines is an example of within-slice correction.

giving the rate of nutation of magnetization around a constant RF field of that value.<sup>9</sup> The current in the transmit coil required to achieve this value of RF field depends on the  $Q$ <sup>10</sup> of the coil.  $Q$  is determined mostly by power losses in the subject, caused mostly by its electrical conductivity, rather than by losses in the coil itself. As the subject is moved into the coil its conductivity loads the coil, and a greater current and hence voltage is required to produce a given  $B_1$  value. The amount of coil loading (i.e. the amount of power which is removed from the coil and is deposited in the subject) varies from subject-to-subject. The loading often also depends on how far into the coil the subject is placed (the shoulders can provide a substantial amount of loading, as they come near to the end of the coil). The pre-scan procedure sets out to obtain the same value of  $B_1$  (and hence FA), regardless of the loading produced by the particular subject.

The transmitter output is adjusted, either manually or automatically, by adjusting attenuators in the amplifier. If the stated values of the attenuator are to be used (for example for a reciprocity correction to determine the receive sensitivity in PD or MRS studies), then their values need to be known to within 1%.<sup>11</sup> Their accuracy should be checked with the manufacturer. The values can be determined directly, using the same procedure as for checking transmitter linearity (see below). In spectroscopy, values of transmitter gain (called TG<sup>12</sup> on General Electric systems) have been used to make reciprocity corrections in the calculation of metabolite concentrations, without any reports of failure (see Figure 4.4).

Nonlinearity in the transmitter output stage may occur, leading to incorrect  $B_1$  values, and distortion

<sup>9</sup> The nutation rate is  $\gamma B_1 \text{ rad s}^{-1}$ ; thus an RF field of 10  $\mu\text{T}$  corresponds to 2680  $\text{rad s}^{-1}$  or 426 Hz.

<sup>10</sup>  $Q$  stands for *quality factor*, denoting how long a coil will ring for after being excited. High- $Q$  coils are less damped, lose less energy per cycle, ring for longer, provide a greater  $B_1$  for a given current and provide a greater signal for a given amount of precessing magnetization.

<sup>11</sup> One per cent is 0.086 dB. Thus uncertainty of 0.1 dB, or 1 TG unit on a General Electric machine, is just tolerable.

<sup>12</sup> On a General Electric scanner the transmitter output is characterized by TG (transmitter gain); the transmitter voltage  $\propto 10^{\text{TG}/200}$  (see also Figure 2.14).

of selective pulses and the resulting slice profiles. Hua and Hurst (1995) reported a 25% reduction at high output levels, and Figure 2.14 shows signs of transmitter overload. Such gross nonlinearity over the normal range of amplitudes of the selective pulses would probably be picked up as artefacts in the routine imaging (depending on the amplitudes of the selective pulses used). Calibration of the transmitter output stage is usually carried out periodically as part of routine preventive maintenance (Venkatesan *et al.*, 1998). Transmitter linearity can be investigated as follows: an oscilloscope can be used to measure the output voltage as a function of software hard pulse amplitude (Alecci *et al.*, 2001); this will be accurate to within a few per cent, depending on the oscilloscope. The output can be stepped by the software for convenience (Tofts *et al.*, 1991a,b). A more accurate method is to use NMR to measure the  $B_1$  amplitude, as follows. At each amplitude, observe the signal from a small sample as a function of hard pulse duration. The null duration gives an accurate and precise measurement of  $B_1$ . Ensure there is no pulse droop, using an oscilloscope. A plot of  $B_1$  vs software pulse amplitude should be linear.

RF nonuniformity is the largest cause of error in qMR.

*Radiofrequency field inhomogeneities are the most irksome sources of nonidealities (especially as a result of their omnipresence). The spatial variation of the RF field sensitivity of the transmit and receive coils enter [sic] the signal expression for any sequence in the form of altering the flip angle at a given spatial location as well as altering the received signal from [the same] spatial location. (Haacke et al., 1999, p. 661.)*

Even at 1.5T the effect is noticeable (see Figures 2.1 and 2.2 and at higher fields the problem becomes worse (see Figure 3.9). An elliptical object (such as the head) in a circularly polarized coil gives a diagonal nonuniformity pattern (Sled and Pike, 1998). At 3T a 20% reduction in  $B_1$  was measured at the periphery of the brain using a birdcage coil (Alecci *et al.*, 2001). Anatomically accurate models of  $B_1$  distribution in the head, using detailed anatomical knowledge (Collins and Smith, 2001; Ibrahim *et al.*, 2001), show that at

high fields, up to 8T, nonuniformity increases as dielectric resonance increases the sensitivity near the centre of the head. The feared reduction in RF penetration at high frequencies (the ‘skin effect’), caused by the electrical conductivity of the tissue, is not large enough to offset the amplifying effect of dielectric resonance (which increases  $B_1$  in objects whose size is comparable with the half-wavelength of electromagnetic waves at the frequency of observation; Figure 3.9). Measurements in the human head at 7T have been reported (Collins *et al.*, 2002). Adjustment of the voltage applied to each port on the coil, and its phase, may allow uniformity to be optimized (Ibrahim *et al.*, 2001). This has been termed ‘RF shimming’.

With the moves towards smaller, close-fitting multiarray coils for better SNR, and towards higher fields, the problems of transmit (i.e.  $B_1$ ) and also receive homogeneity (see Section 2.1.8) will increase. There is a contribution to transmit nonuniformity from the excitation coil, which can be reduced by using the larger body coil for excitation,<sup>13</sup> and a contribution from the head itself, which is present even in a uniform excitation field (see Figure 2.1). Thus there is a value in measuring both the uniformity of the coil (with a large oil phantom), and the RF field *in vivo* (which can be used to aid various measurements).

The longitudinal variation of  $B_1$  along the coil axis can be compensated for by adjusting the transmitter voltage for each axial slice in a multi-slice dataset (Clare and Jezzard, 2001). However receive nonuniformity may still be a problem, and nonuniformity within the slice is not removed.

## 2.1.6 Slice Profile Variations

The slice profile depends on the FA at the slice centre; as the local FA  $\theta$  varies with location, because of  $B_1$  nonuniformity, this in turn alters the area under the slice profile, and also its shape (see Figure 2.3 or a bit later). Ideally the area, and hence signal, vary as  $\sin \theta$  (for a gradient echo), and this is the assumption made in modelling the

<sup>13</sup> Using the body coil may have downsides: increased power deposition (specific absorption rate, SAR), and possibly increased signal from tissue outside the brain.

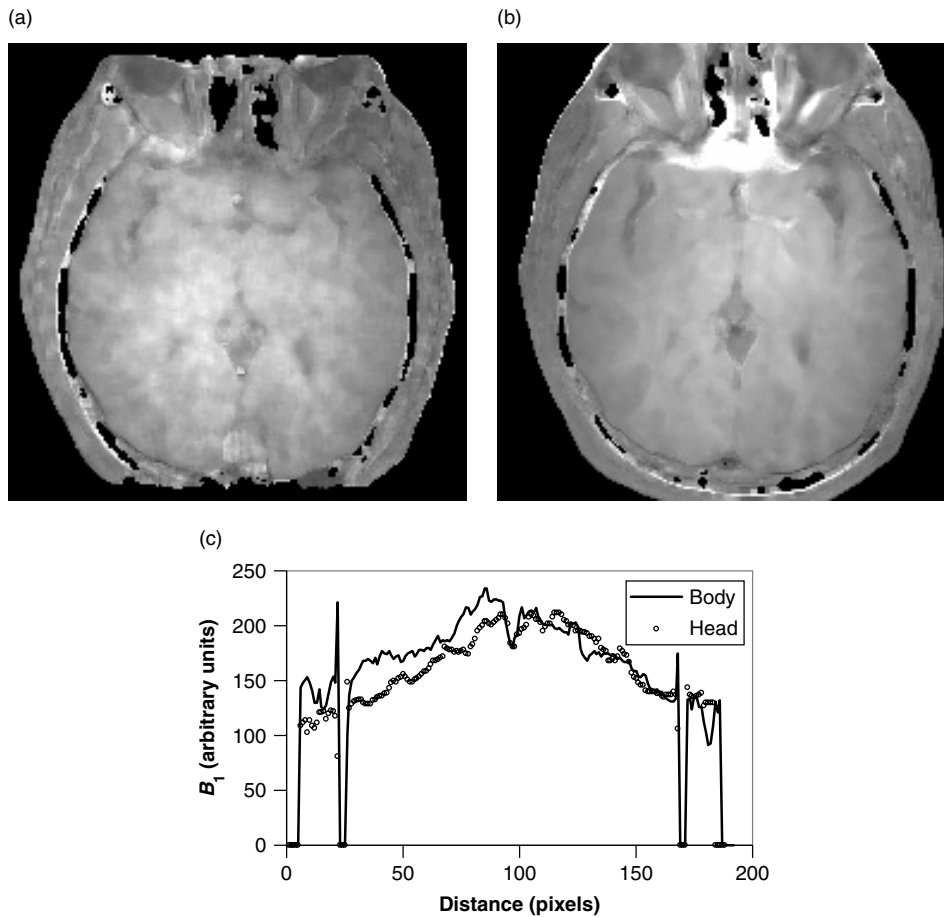


**Figure 2.1.**  $B_1$  field maps in the head in a birdcage coil at 1.5 T. The method of Insko and Bolinger (1993) was used, with  $\theta_1 = 60^\circ$  and  $\theta_2 = 120^\circ$ . (a) Using the relatively uniform body coil for transmission; the observed RF nonuniformity (c) is caused only by the electromagnetic properties of the head. (b) Using the relatively nonuniform head coil for transmission. Extra nonuniformity is seen (in addition to that caused by the head, as seen in part (a), caused by the head coil). The images have been scaled to have approximately the same maximum value. The increased  $B_1$  near the centre of the head is caused by dielectric resonance (RF standing waves); (see also Table 3.4, and Figures 2.2 and 3.9). This outweighs any decrease caused by the skin effect (which would decrease  $B_1$  at the centre, as a result of electrical conductivity in the head). Data courtesy of Dr Lizann Bolinger

effect of FA on signal. In practice, the slice profile has to be modelled explicitly, since there is a distribution of FAs across it. The situation is made more complex if  $T_1$ -weighting is present, because the signal then has a further dependence on the FA at each point in the slice profile, and further distortion is introduced into the slice profile (see Figure 2.4). Examples can be seen in calculations of  $T_1$  (see Parker *et al.*, 2001 and Chapter 1).

Such calculations are not necessary in a three-dimensional (volume) acquisition, where explicit slice selection is not used (although there may be a broad ‘slab selective’ pulse used, which should be taken account of). The steps needed to calculate the slice profile are given below.

Some slice-selective pulses give good profiles, almost rectangular, with little variation of FA across the profile (Pauly *et al.*, 1991), and for these

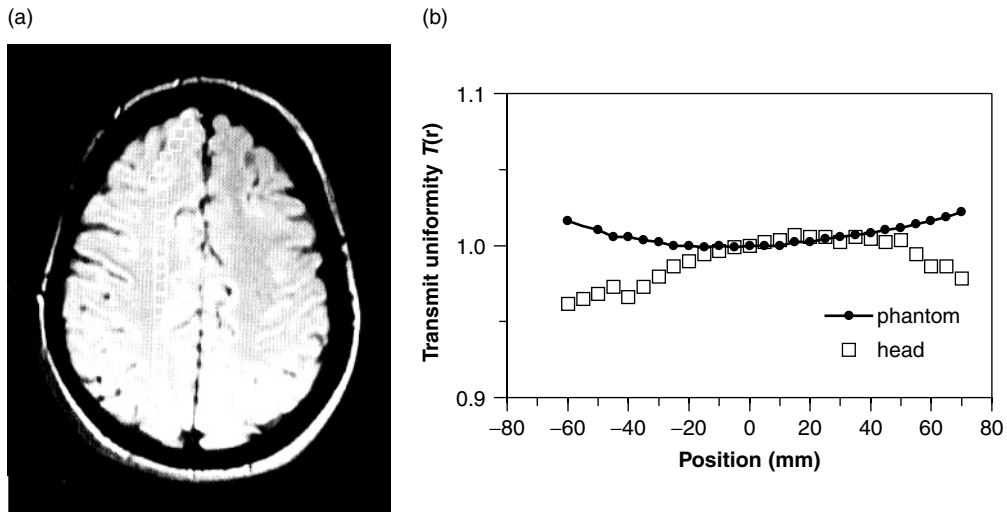


**Figure 2.2.**  $B_1$  variation in the head, imaged at 1.5 T with a four-element birdcage coil. (a) A series of ROIs in the head, from posterior (negative position, at the bottom of the image) to anterior (positive position). (b) Head  $B_1$  values peak at the centre of the head. Equivalent ROIs in a large oil phantom show the opposite effect, with largest  $B_1$  values nearer to the coil elements. This shows that  $B_1$  nonuniformity in the head cannot be measured using a separate phantom, and that methods for measuring  $B_1$  *in vivo* are required. Note the need to avoid placing ROIs in CSF, since  $TR$  was only 2 s. Part (b) was redrawn from data supplied by Professor Barker from Barker *et al.* (1998)

pulses an explicit correction may be unnecessary (although the vulnerability to  $B_1$  changes should be considered). Numerically optimized pulses with a time-varying slice-selection gradient have also been designed. The approach can be used to optimize various factors, such as peak power or within-slice homogeneity. Typical selective pulse design procedures would include pulses for gradient echo excitation (i.e.  $\theta \leq 50^\circ$ ), spin echo excitation ( $\theta = 90^\circ$ ), inversion ( $\theta = 180^\circ$ ) and refocusing ( $\theta = 180^\circ$ ). Slice profiles will suffer if any of these pulses are operated away from their design FAs. The gradient echo pulse will give a reasonable slice profile for small variations in  $B_1$  (since it is operating where the Bloch equations are reasonably linear). Slice profiles will suffer if any of these pulses are operated away from their design FAs.

The Bloch equations can be used to calculate the actual slice profile given by any shaped pulse, of given amplitude, applied in a specified field gradient. The evolution of the magnetization, with a particular temporal resolution, is calculated at many positions within the slice (Joseph *et al.*, 1984;

Fernandez-Seara *et al.*, 2001). A Bloch simulator will usually produce graphs of the magnetization vector ( $M_x^s$ ,  $M_y^s$  and  $M_z^s$ ) after the selective pulse has been applied. The MRI manufacturers provide such simulators, and building one is not too difficult. Saturation effects and longitudinal recovery between pulses are not explicitly modelled (it is assumed that  $M_z^s = 1$  before the pulse is applied).  $T_1$  and  $T_2$  values are used to allow for relaxation effects during the pulse; these effects are usually small.

The procedure for calculating the signal from the whole slice is as follows (Parker *et al.*, 2001):

- (1) At each position<sup>14</sup> in the slice ( $z$ ), calculate the FA  $\theta(z)$  and the phase<sup>15</sup>  $\phi(z)$  from the simulator output:

$$\theta(z) = \tan^{-1} \frac{\sqrt{M_x^s(z)^2 + M_y^s(z)^2}}{M_z^s(z)}$$

<sup>14</sup>  $Z$  denotes distance along a line perpendicular to the slice plane.

<sup>15</sup> The phase  $\phi$  defines the direction of the transverse magnetization in the  $xy$  plane. Here,  $\phi = 0$  corresponds to the  $x$ -axis.

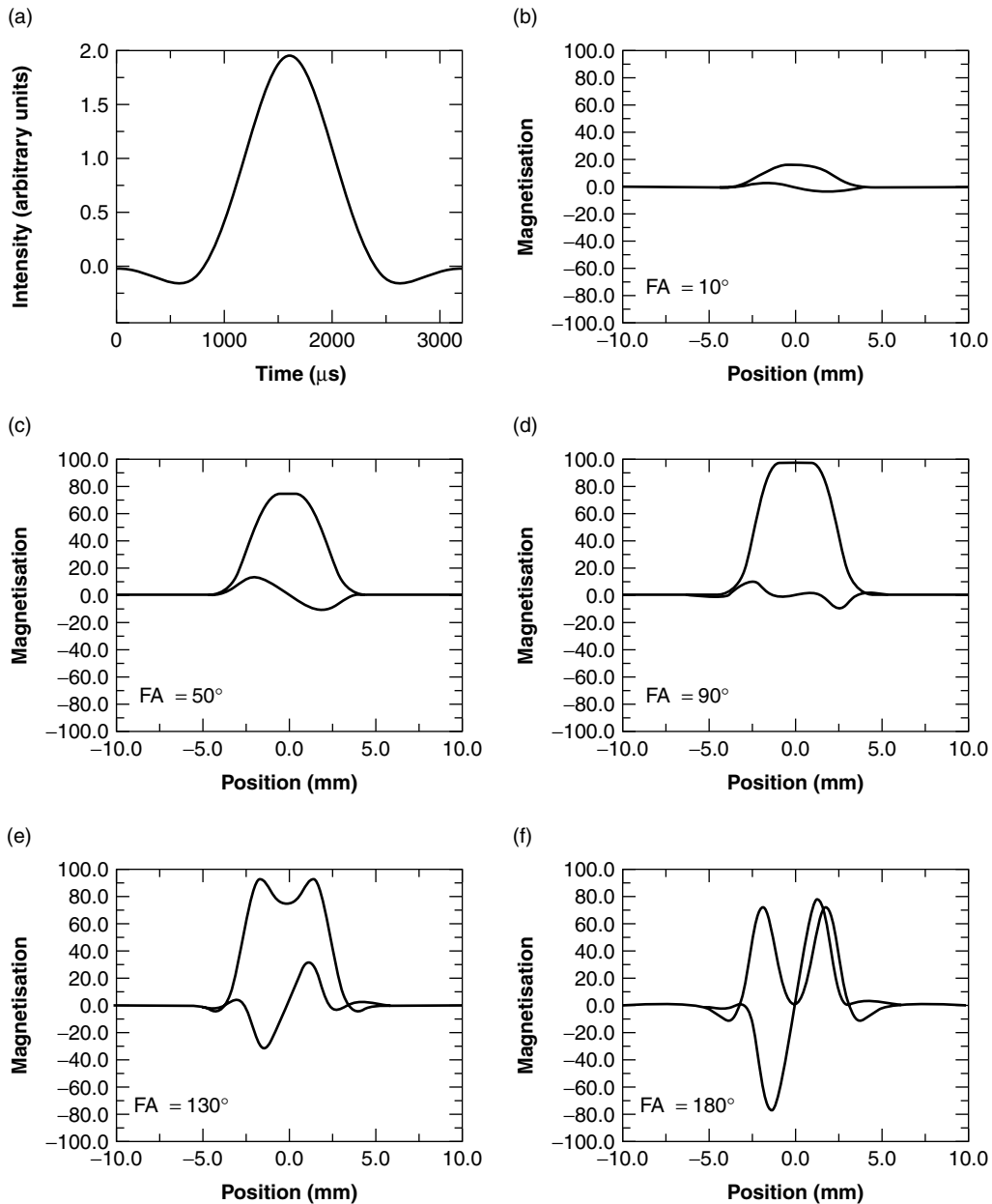


**Figure 2.3.** The effect of incorrect  $B_1$  value on slice profile. A Bloch simulation of a 3 ms selective pulse (a), designed to give 5 mm slice thickness when used with a  $90^\circ$ FA. Thick trace,  $M_x$ ; thin trace,  $M_y$ . The magnetization as a fraction of  $M_0$  is shown. The pulse gives the most rectangular slice profile when the FA at the slice centre is  $90^\circ$ . At other angles the profile is distorted, and much of the sample experiences values of FA different from the nominal one. These simulations are all for relaxed behavior. Saturation by  $T_1$  effects can distort the profiles even further (see Figure 2.4), and can be modelled [see Equation (2.4)]. Reprinted with permission from Parker, G. J., Barker, G. J. and Tofts, P. S. 2001, Accurate multislice gradient echo  $T(1)$  measurement in the presence of non-ideal RF pulse shape and RF field nonuniformity, in *Magn. Reson. Med.*, Copyright 2001 John Wiley & Sons Inc.

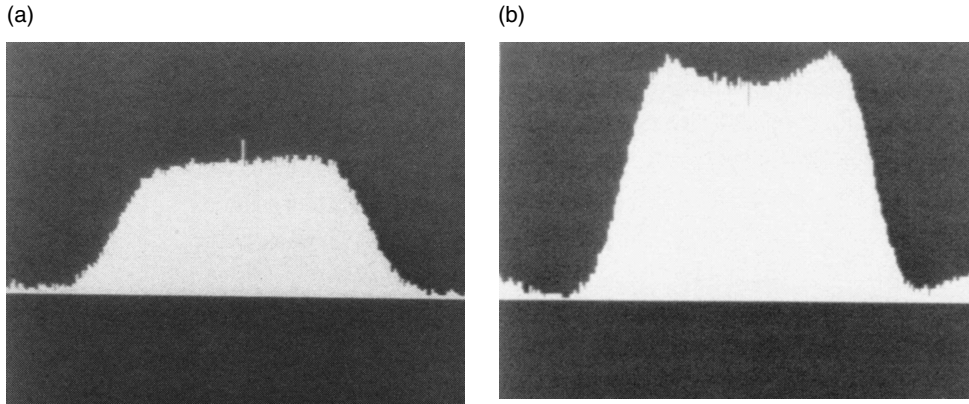


**Figure 2.4.** Slice profile distortion caused by  $T_1$ -weighting. Slice profiles in small phantoms, for a sinc selective pulse,  $TR = 150$  ms, nominal FA =  $40^\circ$ . (a) Nearly relaxed ( $T_1 = 150$  ms); (b) heavily  $T_1$ -weighted [ $T_1 = 1500$  ms; vertical scale increased by 8 compared with (a)]. Protons in the central portion of the slice have greater FAs than the Ernst angle, and thus suffer signal loss, whilst those nearer the edge have lower FAs, close to the Ernst angle, and therefore give a higher signal (the Ernst angle is defined in Figure 2.7). Reprinted with permission from Young, I. R. and Payne, J. A. 1987, Slice-shape artifact changes with precession angle in rapid MR imaging, in *Magn. Reson. Med.*, Copyright 1987 John Wiley & Sons Inc.

$$\phi(z) = \tan^{-1} \frac{M_y^s(z)}{M_x^s(z)} \quad (2.3)$$

- (2) Calculate the actual local transverse magnetization ( $M_x$  and  $M_y$ ), taking into account saturation. For a gradient echo this is:

$$\begin{aligned} M_x(z) &= \frac{M_0(1 - e^{-TR/T_1}) \sin \theta(z)}{[1 - \cos \theta(z)e^{-TR/T_1}]} \cos \phi(z) \\ M_y(z) &= \frac{M_0(1 - e^{-TR/T_1}) \sin \theta(z)}{[1 - \cos \theta(z)e^{-TR/T_1}]} \sin \phi(z) \end{aligned} \quad (2.4)$$

where  $M_0$  is the equilibrium magnetization. Consider a voxel, with in-plane pixel area  $A_{\text{pix}}$ . A thin slab of the voxel, thickness  $dz$ , has volume  $\delta v_s = A_{\text{pix}} dz$ . Using Equation (1), the signal from this slab is:

$$\begin{aligned} \delta v &= g(\mathbf{r}) M_{xy} A_{\text{pix}} dz \\ g(\mathbf{r}) &= \omega_0 B_{1xy} \cos(\omega_0 t) \end{aligned} \quad (2.5)$$

where  $g(\mathbf{r})$  is the local gain (i.e. the signal per unit magnetization and volume). The signal from the  $x$ - and  $y$ -components of the magnetization is then formed by integration over the

slice profile, and the magnitude signal from the whole slice is then

$$\begin{aligned} S &= g(\mathbf{r}) A_{\text{pix}} \left[ \left( \int_{-\infty}^{\infty} M_x(z) dz \right)^2 \right. \\ &\quad \left. + \left( \int_{-\infty}^{\infty} M_y(z) dz \right)^2 \right]^{1/2} \end{aligned} \quad (2.6)$$

In some situations the out-of-phase component ( $M_y$ ) can be ignored, if it integrates to zero across the slice (see Figure 2.4). However, the phase shift  $\phi$  must still be considered, as it causes a reduction in the in-phase component  $M_x$ , by the factor  $\cos \phi$  [see Equation (4)]. The integral in Equation (6) is evaluated as a summation.

Having obtained the total signal, with the unknown constants  $M_0$  and  $g(\mathbf{r})$  in the expression, it can be used in several ways. An effective slice thickness<sup>16</sup>  $t_{\text{eff}}$  can be found from the ratio of the total signal to the signal per unit slab thickness at

<sup>16</sup> This definition of effective slice thickness serves to characterize the total signal received from the slice. An alternative definition could be made, characterizing its spatial extent (for example, its full-width half-maximum).

the slice centre  $s_0$ .

$$s_0 = \frac{g(\mathbf{r})A_{\text{pix}}M_0(1 - e^{-TR/T_1}) \sin \theta_0}{(1 - \cos \theta_0 e^{-TR/T_1})}$$

$$t_{\text{eff}} = \frac{S}{s_0} \quad (2.7)$$

where  $\theta_0$  is the FA at the centre of the slice. In calculating  $t_{\text{eff}}$ , its value depends only on the simulator output magnetization ( $M_x^s$ ,  $M_y^s$  and  $M_z^s$ ),  $T_1$  and  $TR$ ; the factors  $g(\mathbf{r})$ ,  $A_{\text{pix}}$  and  $M_0$  divide out. The variation over space of this effective slice thickness, as  $B_1$  and hence  $\theta_0$  vary over space, gives the change in slice sensitivity over space. For each value of  $B_1$ , the simulator must be re-run to obtain a new relaxed slice profile. Near the FA for which the pulse was designed, the slice profile will be good, and the effective slice thickness close to its design value, whilst further away from the design FA, performance will suffer and effective slice thickness will alter (see Figure 2.3 and also Figures 2.5 and 2.6). Note that the ‘nominal FA’, set by the scanner in an autopre-scan procedure, will not in general equal  $\theta_0$  (although it may be close if the slice profile is close to rectangular in shape, and uniformity is good).

It should be born in mind that this approach to dealing with slice profile is based on a model and simulation: reality can be altered by such effects as transmitter nonlinearity, incorrect FA settings, gradient eddy currents, relaxation during the pulse, unspoilt transverse magnetization, and magnetization transfer. Slice profile calculation is also discussed in Chapter 5, in the context of the determination of  $T_1$ .

## 2.1.7 $B_1$ Field Mapping

The determination of the RF field  $B_1$  at each location in space is important for two reasons. First, its value is needed for accurate measurement of some MR parameters (e.g. magnetization transfer, MT). A determination of its nonuniformity (if uncorrected) enables the resulting errors in the parameter to be estimated. Second, knowledge of the  $B_1$  map enables spatial variation in the receive sensitivity to be corrected, using the principle of reciprocity (see Section 2.1.9).

### 2.1.7.1 Principles of $B_1$ Mapping

Early methods of determining FA, or setting it to a required value, were developed in spectroscopy. A sample inside a uniform RF coil gives

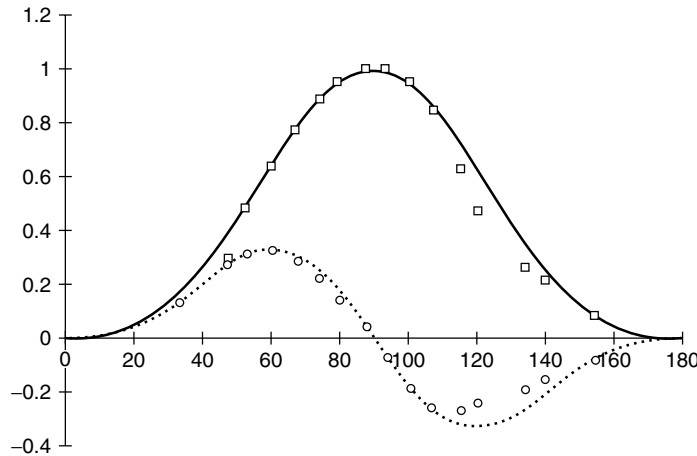


**Figure 2.5.**  $B_1$  mapping by the ratio of stimulated echo to spin echo signals. Signals from spin echo (upper trace) and stimulated echo (lower trace) vs FA (calculated from theoretical fit). At high FAs, the measured signal is reduced by slice profile effects. Reprinted Akoka, S., Franconi, F., Seguin, F. and Le Pape, A. 1993, Radiofrequency map of an NMR coil by imaging, in *Magn. Reson. Imag.* **11**, 437–441, Copyright 1993 with permission from Elsevier Science Ltd

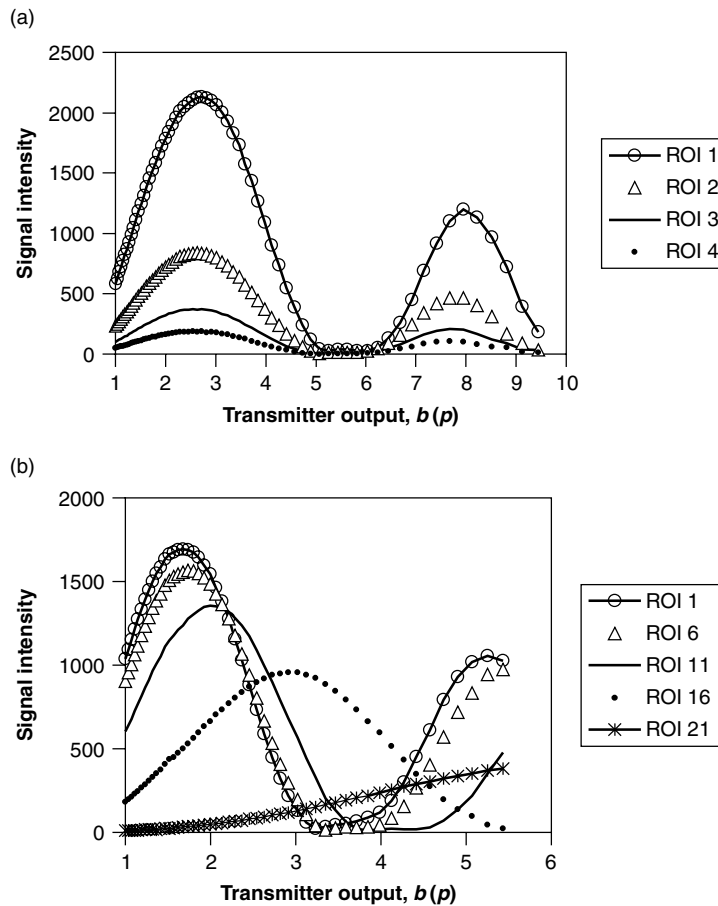


**Figure 2.6.** Spin echo signal vs transmitter voltage.  $b(p)$  is the transmitter voltage in arbitrary units. Measurements are shown at several ROI locations in a large uniform oil phantom. (a) Extremely uniform excitation (body coil excitation, surface coil reception). ROI 1 is nearest the surface coil, ROI 4 is furthest away. Regions further from the surface coil have less signal. The transmitter output to produce a  $180^\circ$  pulse, as seen by the signal null at  $b = 5.7$ , is independent of ROI location (since the excitation field is uniform). The second (right-hand) peak in signal is lower than the first, because of slice profile effects; these become worse at high FA, and the signal ceases to follow the theoretical  $\sin^3 \theta$  dependence. Note that in the case of *in vivo* imaging, a reduction in signal caused by coil sensitivity could not be distinguished from a reduction caused by decreasing proton density, unless the coil sensitivity is determined separately using the principle of reciprocity. (b) Extremely nonuniform transmission (head coil excitation and reception). Regions are at the periphery of the coil, and outside it. Region 1 (nearest to centre) has highest peak signal, and lowest transmitter output to achieve null signal ( $b = 3.4$ ). Outer regions have progressively lower signal peak (reduced reception sensitivity), and need a higher transmitter voltage to achieve a null signal [these regions have a lower transmit ( $B_1$ ) field]. Redrawn from data supplied by Professor Barker from Barker *et al.* (1998)

a maximum signal when the FA is  $90^\circ$ , provided it can relax fully between pulses (i.e.  $TR \gg T_1$ ). The pulse amplitude,<sup>17</sup> or duration, is increased from

<sup>17</sup> A rectangular pulse, of amplitude  $B_1$  and duration  $\tau$ , produces a FA of  $\gamma B_1 \tau$ . Depending on the spectrometer

hardware, either the pulse amplitude or duration is varied to give the required FA. Early spectrometers had fixed amplitude, and the duration was altered. Modern MRI machines often fix the duration (since this fixes the bandwidth and the spatial selection), and allow the amplitude to be altered.

a low value; at first the signal increases almost linearly, then reaches a maximum, then declines. Further increase in the pulse gives a null signal (corresponding to a FA of  $180^\circ$ ), and this condition can often be found more precisely than the maximum at  $90^\circ$ .

Although a number of methods have been published, they can all be reduced to addressing two fundamental issues. First, what pulse or pulses are used to generate a signal, or a ratio of signals, that depends only on the local FA (and is independent of the usual confounding factors such as PD,  $T_1$  and  $T_2$ )? This can be viewed as the magnetization preparation stage. Second, how can the three-dimensional distribution of magnetization that has been created be read out without incurring errors caused by the inevitable uncertainty in the value of the local FA? Currently none of the published sequences can produce a  $B_1$ -map over the whole brain, in a reasonable time, free from potential slice profile errors (although several are close).

Ideally a hard nonselective (rectangular) pulse is used for the initial magnetization preparation, yet this makes read-out less straightforward. Many workers have used selective pulses, but the resulting measurements are always vulnerable to slice profile errors. As the FA  $\theta$  is altered, the area under the slice profile does not vary as the  $\sin\theta$  or  $\sin^3\theta$ , as we would expect for a relaxed gradient echo or spin echo; instead it deviates, particularly as  $\theta$  becomes much less than or greater than the value for which the slice-selective pulse was designed (see Figure 2.4 and Section 2.1.6). Applying a hard pulse (as opposed to a selective pulse) may be difficult with the pulse sequence software that scanners have on them. The spectroscopy sequences are often the most useful, possibly as starting points for a modified sequence, because they already make use of hard pulses (see for example Chapter 9, Figure 9.5. If an existing sequence is to be used, it may be impossible to avoid slice-selective magnetization preparation.

The published sequences use two approaches to varying the FA. In the first,  $B_1$  is altered, and thus all the pulses in the sequence, including those intended for image readout, are affected (Table 2.2; scheme B, Section 2.1.7.2.2). In the second, only

the magnetization preparation pulses are altered, whilst the readout part of the sequence is kept fixed (Table 2.1; schemes A and C, Section 2.1.7.2.1 and 2.1.7.2.3). Thus in the second approach no errors result from the use of selective pulses for readout.

Transmitter nonlinearity in the output stage is a possibility, particularly at high output voltages (Hua and Hurst, 1995, Venkatesan *et al.*, 1998). Any such behaviour will distort a plot of signal vs  $B_1$  value. To avoid this problem,  $B_1$  mapping is best carried out at voltages similar to those used for *in vivo* imaging, and well away from maximal values, although the resulting pulses may be rather long and their limited bandwidth may make them vulnerable of off-resonant effects. The ideal would be to use short high-amplitude pulses with an amplifier proven to be linear. Failure of the signal to follow model behaviour has often been ascribed to slice profile alterations, but there may also be a contribution from transmitter nonlinearity.

Many of the published schemes have TRs that allow reasonably complete relaxation for white and grey matter, but are too short for CSF; thus  $B_1$  values determined in CSF may be inaccurate (see Figure 2.2). However, some of the schemes described below do not require complete relaxation. Note that, although the signal maxima are distorted by  $T_1$  relaxation, the positions of the minima (at  $180^\circ$  etc.) are unchanged Figure 2.7 (see also Figure 2.8).

The choice of nominal FAs for the  $B_1$  mapping scheme will depend on the how nonuniform the  $B_1$  field is. A small range can be covered by two values; a larger range may require several values (although with skilful tracking of  $B_1$  from pixel to pixel, two values can be used over a wide dynamic range, close to the wires of the RF coil; Insko and Bolinger, 1993).

### 2.1.7.2 Pulse Schemes

#### 2.1.7.2.1 Scheme A: One Pulse Read $M_{xy}$

A single pulse is applied, then the signal from the transverse magnetization  $M_{xy}$  is observed. The signal dependence is  $\sin\theta$ . Thus if two pulse

**Table 2.1.** Major RF field  $B_1$ -mapping techniques

Technique	Details	Signal dependence	Hard or selective magnetization preparation	Publications	Observations
A: one pulse, $M_{xy}$	2-(readout $M_{xy}$ )	$\sin 2$	Hard	Hornak <i>et al.</i> (1988)	
			Selective	Stollberger <i>et al.</i> (1988); Fernandez-Seara <i>et al.</i> (2001)	$(\theta/2, 2\theta)$ , $(\theta, 2\theta)$ spin echoes
			Selective	Insko and Bolinger (1993)	see Figure 2.1
			Selective	Stollberger and Wach (1996)	Faster version of 1988 version
B: spin echo	2-22-echo	$\sin^3 2$	Hard	Venkatesan <i>et al.</i> (1998)	$160^\circ < \theta < 210^\circ$ three-dimensional grad echo (see Figure 2.8)
			Selective	Hornak <i>et al.</i> (1988)	
			Selective	Insko and Bolinger (1993)	
C: one pulse $M_z$	2-spoil-(readout $M_z$ )	$\cos 2$	Selective	Barker <i>et al.</i> (1998)	Multiple $\theta$ s to plot $\sin^3$ function (see Figure 2.6)
			Hard	Topp <i>et al.</i> (1997)	See Figure 2.9
			Hard	Pan <i>et al.</i> (1998) Sled and Pike (2000) Vaughan <i>et al.</i> (2001)	Two close pulses Hard pulse + FSE See Figure 2.10

amplitudes, of  $\theta$  and  $2\theta$  are used, the ratio of the second signal to the first is  $\sin 2\theta / \sin \theta = 2 \cos \theta$ . At low  $\theta$ ,  $\cos \theta \approx 1$  and the ratio is insensitive to  $\theta$  (the signal is linearly related to  $\theta$ ). To measure  $\theta$ , a larger value must be used, where  $\sin \theta$  is nonlinear with  $\theta$ . If  $\theta$  exceeds  $90^\circ$ , the signal decreases, and  $\cos \theta$  becomes multi-valued.<sup>18</sup> Thus  $\theta$  must be chosen carefully: too small and the ratio of signals is insensitive to  $\theta$ ; too large and unwrapping is required.

Reading the transverse magnetization after a hard nominal  $90^\circ$  pulse may be difficult, since it gives a large signal from the whole sample. A slice-selective  $180^\circ$  pulse has been used in a qualitative scheme (Zelaya *et al.*, 1997). A

<sup>18</sup> That is, there are several possible values of  $\theta$  that all have the same value of  $\cos \theta$ .

three-dimensional gradient echo phase-encoding scheme (Talagala and Gillen, 1991) is slow.

Conventional gradient echo (and also spin echo) imaging, with two values of  $B_1$ , has been used by Hornak *et al.* (1988), who demonstrated qualitative agreement with results using a RF pickup coil. Insko and Bolinger (1993) demonstrated imaging in a thin phantom (where no slice selection was required). The gradient echo  $\sin \theta$  function was preferred to the spin echo  $\sin^3 \theta$  function because of its wider range.

The crucial step of altering the preparation pulse (i.e. the first one), whilst keeping the readout pulse (the second one) fixed, was taken by Stollberger *et al.* (1988), who used sequences with selective pulses to form a spin echo. The sequences were  $(\theta/2, 2\theta)$  and  $(\theta, 2\theta)$ , with a nominal value of

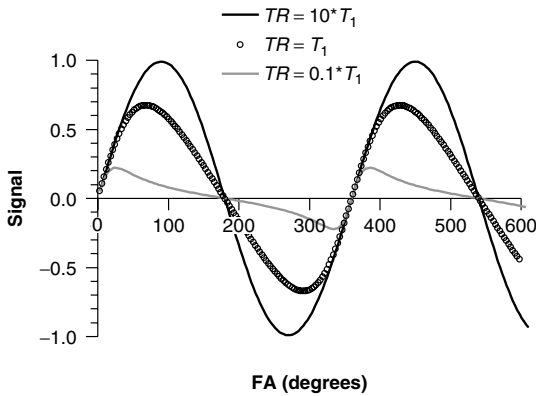


**Figure 2.7.** The effect of  $T_1$  relaxation on the cyclical variation of gradient-echo signal with FA. At long  $TR$  the classic sine behaviour is seen, with a maximum at  $90^\circ$  and a null at  $180^\circ$ . As  $TR$  is shortened, the position of the maximum shifts to the left (the Ernst angle effect), whilst the position of the null is unaffected. In this simulation, the signal  $S = [1 - \exp(-TR/T_1)] \sin \theta / [1 - \cos \theta \exp(-TR/T_1)]$ . Slice profile effects have been ignored.  $S$  has a maximum at  $\cos \theta_E = \exp(-TR/T_1)$ , and this defines the Ernst angle  $\theta_E$ .

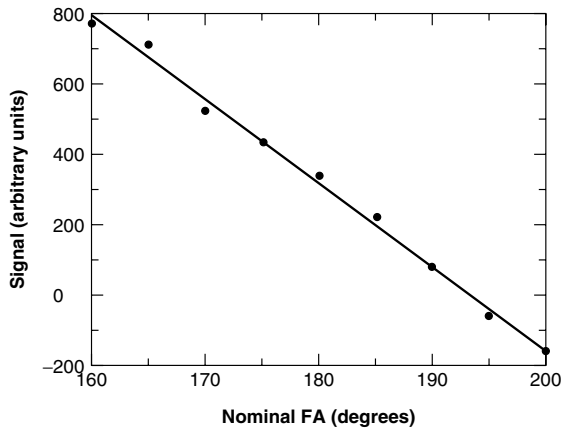


**Figure 2.8.**  $B_1$  mapping using a nominal  $180^\circ$  hard pulse. The signal is plotted vs nominal FA, for a three-dimensional spoiled gradient echo sequence, near the null point. Reprinted with permission from Venkatesan, R., Lin, W., and Haacke, E. M. 1998, Accurate determination of spin-density and  $T_1$  in the presence of RF-field inhomogeneities and flip-angle miscalibration, in *Magn. Reson. Med.*, Copyright 1998 John Wiley & Sons Inc.

$90^\circ$  for  $\theta$ . Thus the second sequence is a conventional spin echo (nominally  $90^\circ, 180^\circ$ ), whilst the first (nominally  $45^\circ, 180^\circ$ ) has a reduced excitation pulse but identical echo formation. The ratio of the signal intensities (second/first) is  $\sin \theta / \sin(\theta/2) = 2 \cos(\theta/2)$ . This method was used by Fernandez-Seara *et al.* (2001) with a fast spin echo (RARE) sequence to produce rapid  $B_1$  maps. With  $TR = 4$  s, 128 phase encodes and an echo train length of 8, two values of  $\theta$  ( $45^\circ$  and  $90^\circ$ ) could be measured in 2 min. The slice profile of the first pulse was found not to vary as its amplitude was changed. A similar method was used by Alsop *et al.* (2001), who collected 10 images with single-shot fast spin echo, varying the initial selective pulse between near zero and  $120^\circ$ , giving a measurement time of under 1 min. A faster version of the original Stollberger proposal used a compensation pulse to return the magnetization to the  $z$ -direction, thus allowing a shorter  $TR$  to be used (Stollberger and Wach, 1996, 1997).

A hard pulse followed by a three-dimensional spoiled gradient echo ( $TR = 25$  ms) was used by Venkatesan *et al.* (1998) to determine the null point (at  $\theta = 180^\circ$ ), from six different nominal FAs ( $160$ – $210^\circ$ ). Near the null point, the absolute (signed) signal varies linearly with  $\theta$  [since  $\sin \theta = \sin(180^\circ - \theta) \approx 180^\circ - \theta$ ]. The use of the null point allows  $B_1$  in CSF to be determined accurately with short  $TR$ . (Figure 2.8). They also determined a map of relative  $B_1$  values, using the same three-dimensional sequence, with a small ( $2^\circ$ ) FA, when the signal is proportional to  $B_1^2$  (since  $\sin \theta \approx \theta$ ).

#### 2.1.7.2.2 Scheme B: Spin Echo (Both Pulses Altered)

A  $(\theta 2\theta)$  sequence gives a signal proportional to  $\sin^3 \theta$  (Hornak *et al.*, 1988), provided it is relaxed (the behaviour is much more complicated if recovery of the longitudinal magnetization has to be included). Insko and Bolinger (1993) demonstrated this with imaging, using phase cycling to eliminate the FID signal from the two pulses. A spin echo ( $\theta, 2\theta$ ) sequence, e.g. with nominal  $\theta = 45^\circ, 90^\circ$  (i.e. half and full amplitude) can be used for this. The ratio of signals from sequences with full and half amplitude is  $8 \cos^3(\theta/2)$  (where  $\theta$  is the FA for

the full amplitude sequence). Barker used a range of  $B_1$  values to plot the cyclical variation of signal in a slice selective spin echo (Figure 2.6), and the approach has also been used by Alecci *et al.* (2001). Although the spin echo approach is easy to implement, its vulnerability to slice profile error (because the  $180^\circ$  readout pulse is altered in amplitude) limits its accuracy.

### 2.1.7.2.3 Scheme C: One Pulse Read $M_z$

Instead of measuring the transverse magnetization after a single pulse, this method looks at what is left of the longitudinal magnetization after a single pulse. This overcomes the difficulties of trying to read the transverse magnetization after a hard pulse, as in scheme A.

Topp *et al.* (1997) produced an ingenious solution, in the form of a hard pulse embedded in a selective STEAM sequence; this destroys the

part of the magnetization which is stored in the  $z$ -direction during the second interval of the stimulated echo. Spoiler and crusher gradients were carefully placed to avoid unwanted coherences. Special care was taken to avoid signals induced by the hard pulse. The fit to the theoretical cosine function was extremely close, thanks to the use of the hard pulse instead of a slice selective scheme, with  $B_1$  determined to better than 1 % (Figure 2.9). Seven slices were imaged in 2 min, and the authors point out the potential to use echo planar imaging (EPI) or spiral readout for further reduction of imaging time. The method has also been used by Sled and Pike (1998).

Pan *et al.* (1998) used two selective pulses, of nominal value  $60^\circ$ , separated by only 25 ms, to acquire low-resolution gradient echo images. The ratio of signals (second to first) was  $\cos \theta$ . Slice profile effects were taken into account. This sequence can be run at short  $TR$ , but to minimize

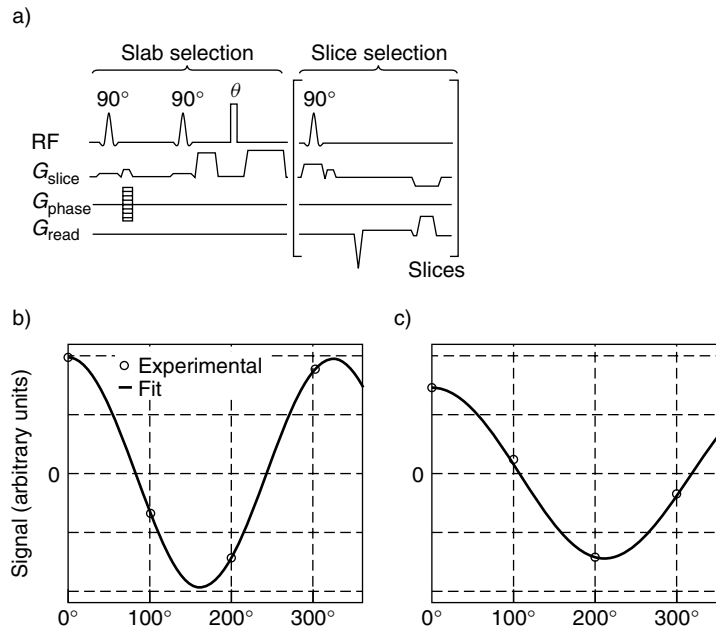


**Figure 2.9.** (a) Hard two-pulse and spoiler inserted into a STEAM imaging sequence. (b) Signal vs nominal FA  $\theta$ , near the centre of a 28 cm aqueous cylinder at 1.5 T. (c) Signal near the periphery of the same phantom. Note the minimum comes at a larger nominal FA (i.e. more power must be applied to achieve an FA of  $180^\circ$  at this location), and that the signal is reduced (in accordance with the principle of reciprocity). From Topp, S., Adalsteinsson, E. and Spielman, D. 1997, Fast multislice  $B_1$ -mapping, in *Proc. Int. Soc. Magn. Reson. Med.* Copyright 1997 Reproduced by permission of ISMRM

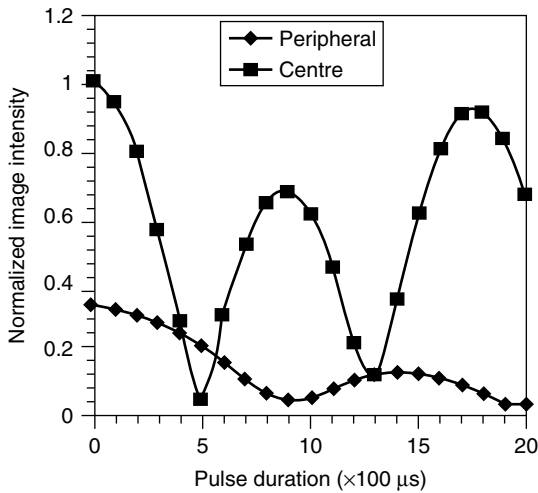


**Figure 2.10.** Signal after a single hard pulse, using the ‘one pulse  $M_z$ ’ scheme C, at 7 T. The signal is proportional to  $\cos\theta$ ; thus the first minimum occurs where the local FA =  $90^\circ$ . At a duration of 500  $\mu\text{s}$  the pulse gives a flip angle of  $90^\circ$  at the centre of the brain (upper trace), corresponding to  $B_1 = 14 \mu\text{T}$  (for a standardized 1 kW pulse power). At the periphery of the brain a duration of 900  $\mu\text{s}$  is needed to achieve  $90^\circ$ , corresponding to a lower value for  $B_1 = 8 \mu\text{T}$  (lower trace). Reprinted with permission from Vaughan, J. T., Garwood, M., Collins, C. M., Liu, W., DelaBarre, L., Adriany, G., Andersen, P., Merkle, H., Goebel, R., Smith, M. B. and Ugurbil, K. 2001, 7 T vs. 4 T: RF power, homogeneity, and signal-to-noise comparison in head images, *Magn. Reson. Med.*, Copyright 2001 John Wiley & Sons Inc.

the error from recovery during the interpulse interval (25 ms), time for full relaxation should be allowed.

Sled and Pike (2000) used a hard pulse, with nominal values of  $33^\circ$  and  $66^\circ$ , followed by spoiling and a slice selective fast spin echo readout of the remaining  $z$ -magnetization. This gave a  $256 \times 256$  map in 2.5 min, although the  $TR$  of 2 s did not allow CSF to relax. A reduction in matrix size would allow  $TR$  to be increased.

Vaughan *et al.* (2001) measured the  $B_1$  distribution in the head at 4 and 7 T. A hard pulse, with a range of 20 durations, was followed by gradient spoiling. The residual longitudinal magnetization was imaged rapidly using a single-slice



**Figure 2.11.**  $B_1$  fringes with ‘one pulse  $M_z$ ’ scheme C. A hard  $1800^\circ$  pulse followed by two-dimensional gradient echo readout gives  $B_1$  fringes. Light and dark rings occur at intervals of 5% change in  $B_1$ . Dark rings occur at intervals of 10%. For other values of hard pulse FA, the interval is  $(1800^\circ/\text{FA})\%$ . Reprinted with permission from Deichmann, R., Good, C. D. and Turnes, R. 2002, RF inhomogeneity compensation in structural brain imaging, in *Magn. Reson. Med.*, Copyright 2002 John Wiley & Sons Inc.

turboflash (fast gradient echo) collection. The distribution was relatively uniform at 4 T, but at 7 T  $B_1$  values were nearly twice as high in the centre as at the periphery (Figure 2.10).

Deichmann *et al.* (2002) used a high FA hard pulse ( $1800^\circ$ ) followed by spoiling and a fast gradient echo readout to produce fringes (see Figure 2.11), similar to those produced by Zelaya *et al.* (1997) with scheme A. These provide known values of  $B_1$  at the null locations (i.e. the dark rings), and values at other locations could be interpolated. The method can be quick to implement, and no post-processing is required.

#### 2.1.7.2.4 Scheme D: Other Methods

The phase of the signal from a composite pulse ( $90_y 180_x 90_y$ ) is approximately equal to the

actual FA of the central pulse, and this potentially provides a convenient way of measuring a  $B_1$  map (Oh *et al.*, 1990).

The ratio of signals from a stimulated echo and a spin echo is a convenient way of obtaining the absolute FA in a single measurement, and can be run at relatively short  $TR$  (Akoka *et al.*, 1993). The four signals coming from this three-pulse sequence were separated by careful choice of the echo and mixing times. For a  $(\theta-2\theta-\theta)$  sequence, the amplitude of the spin echo is  $k \sin^3 \theta$ , that of the stimulated echo<sup>19</sup> is  $(k/2) \sin^2 \theta \sin \theta$ , and ratio (second to first) is  $\cos \theta$ . Measured intensities showed deviations from theory at high FAs, presumably due to slice profile effects (Figure 2.5).

Combining the four signals from a three-pulse scheme enables  $B_1$  to be estimated (Carlson and Kramer 1990). Counsell (1993) has published a four-pulse scheme for simultaneously measuring several quantities, including  $B_1$ . Multiple coherence pathways lead to nine echo signals and, provided these can be reliably measured, this method is potentially valuable. A three-pulse scheme  $(\alpha-\alpha-\alpha)$  shows a sharp null at  $\alpha = 90^\circ$  (Perman *et al.*, 1989), potentially giving a very precise determination of  $B_1$ .

The  $B_1$  field can be measured directly using a pick-up coil (Fakri-Bouchet *et al.*, 1998; Alecci *et al.*, 2001). This method can in principle provide verification of imaging methods of measuring  $B_1$ , but paradoxically is only applicable for a coil that is nearly empty, or contains liquid, since the pickup coil must have access.

### 2.1.7.3 Implementation

The ideal implementation will use a hard pulse followed by fast readout, and give correct values in CSF. High spatial resolution is not required (values can be interpolated for use with high-resolution images). It may be possible to provide values in CSF by interpolation, in which case the requirements on  $TR$  are substantially relaxed. Using the null signal, with short- $TR$  three-dimensional imaging (see Figure 2.9) is attractive, and gives good

<sup>19</sup> The paper by Akoka *et al.* (1993) has a typographical error for the stimulated echo signal.

precision, provided SAR limits are not exceeded.  $TR$  could be increased, at the expense of matrix size, if necessary. The ‘one pulse  $M_z$ ’ methods also look attractive, and can probably have their coverage and readout speed increased. The stimulated echo methods require good separation of the echoes to be accurate.

The precision and accuracy required are high for PD and MT measurements (about 1%); spectroscopy can probably tolerate worse performance (maybe 3%). Null methods will in general give better precision than other methods.

Scanning time limits most of the currently published methods. It may be possible to model  $B_1$  behaviour in the head well enough (in particular the inter-subject differences) that a detailed measurement is not needed for each *in vivo* study. Although  $B_1$  mapping can correct for poor RF uniformity in some acquisitions (e.g. quantitative MT), it cannot correct for nonuniformity in all situations (e.g. poor localization in MRS caused by a locally incorrect FA).

## 2.1.8 Receive Sensitivity Field

### 2.1.8.1 Alterations in Receive Sensitivity

Three factors can alter the receive sensitivity, and these all need to be taken into account if absolute signal values are important (particularly in PD and MRS).  $B_1$  nonuniformity is discussed further in Section 2.1.5 above.

*Loading of the coil* (discussed in Section 2.1.5 above) can alter the sensitivity across the whole field of view if the sample is changed. It can be corrected by measuring the transmitter voltage  $V_T^\theta$  required to produce a particular FA  $\theta$  at a particular location (usually the coil centre) and using the reciprocity theorem. The product of signal (at any location)  $S(\mathbf{r})$  and the transmitter voltage, under varying loading conditions, is a constant that depends only on position:

$$S(\mathbf{r})V_T^\theta = C_1(\mathbf{r}) \quad (2.8)$$

This type of correction is quick to make (since  $V_T^\theta$  can be measured quickly), and is used in the determination of metabolite concentrations with the linear combination (LC) model (see Chapter 9).

It does make the assumption that the spatial behaviour of the  $B_1$  field is not affected by changes in loading. If this assumption is not valid, then  $V_T^\theta$  should be measured at each location where the corrected signal is required, or alternatively a  $B_1$  map should be acquired.

*Receive nonuniformity* gives a sensitivity  $g(\mathbf{r})$  that varies with position. Reciprocity enables it to be determined from a  $B_1$  map:

$$g(\mathbf{r}) = C_2 B_1(\mathbf{r}) \quad (2.9)$$

where  $C_2$  is a constant;  $g(\mathbf{r})$  is the signal for unit transverse magnetization. These two methods of correction are discussed further in the chapters on PD and MRS (Chapters 4 and 9).

The *receiver gain* can be altered<sup>20</sup> during the pre-scan procedure to account for the magnitude of the signal (this is much reduced in spectroscopy). If the value of the *receiver attenuators* is known accurately, then these values can be used to make corrections to the signal. Alternatively (and preferably), they can be fixed at suitable values that will not overload the receive chain, nor introduce extra noise. Changes in gain introduced by bit shifts after digitization of the signal will be accurate. Receiver attenuator errors of 1.5–2.0 db have been reported (Barker *et al.*, 1993).

### 2.1.8.2 Image Noise

Electrical noise comes from random thermal agitation (Brownian motion) in the subject, the RF coil and possibly the pre-amplifier. With good design, contributions from the hardware are made insignificant and the dominant source is the subject.

#### 2.1.8.2.1 Optimized Sequence Parameters

The effect of image noise can be reduced by careful choice of sequence parameters. Increasing the voxel size reduces noise (at the expense of spatial resolution). Increasing the number of averages (NEX, the number of excitations) reduces

<sup>20</sup> On a General Electric scanner, there are two controls: R1 gives coarse adjustment of the receiver gain, and should be kept fixed, whilst R2 gives finer control by bit-shifting to give changes that are exact powers of 2.

the noise ( $\text{SNR} \propto \text{NEX}^{1/2}$ ). Increasing the  $TR$  often also increases the SNR. Changing NEX or  $TR$  usually increases the acquisition time, and for a fixed acquisition time an optimal combination of parameters can be found which maximizes SNR (Figure 2.12). The acquisition of images from which parameters such as blood–brain permeability are to be estimated can also be optimized (Tofts, 1996; see Figure 2.12).

#### 2.1.8.2.2 Rician Distribution in Magnitude Image Gives Systematic Error

Most images are constructed from the magnitude of the complex image data, and phase information is discarded. Magnitude data does not have a normal distribution (it cannot be negative). At low values of SNR, the distribution follows a Rician probability distribution with a nonzero mean value (Edelstein *et al.*, 1984; Henkelman, 1985, 1986; Gudbjartsson and Patz, 1995; Haacke *et al.*, 1999). At high values of SNR this approximates to a Gaussian (normal) distribution; at zero SNR it becomes a *Rayleigh distribution*. This effect constitutes a systematic error, or bias, in addition to the random error that noise always contributes. It can be seen most clearly by looking at the mean value in air regions of the image, where a nonzero value will be found. If the standard deviation in high SNR regions of the image is  $\sigma$ , then sampling an air region of interest (ROI) will give a mean value of  $1.25\sigma$  and a standard deviation of  $0.66\sigma$ <sup>21</sup> (Figure 2.13). These air values provide a convenient way of measuring the noise  $\sigma$  in the high-SNR regions of the image. Whittall *et al.* (1997) used this method to show that deviations from their model  $T_2$  decay curves were consistent with those expected from image noise. The air ROI should be checked for the absence of systematic image artefacts by setting the centre of the grey level display window to zero to enable the characteristics of the air values to be seen properly. Any artefacts that are visible in the air are of interest, since they almost certainly extend to the high-SNR parts of the image, in the brain.

<sup>21</sup> The exact values are: mean =  $\sqrt{(\pi/2)}\sigma = 1.2533\sigma$ ; SD =  $\sqrt{(2 - \pi/2)}\sigma = 0.6551\sigma$  (Edelstein *et al.*, 1984).

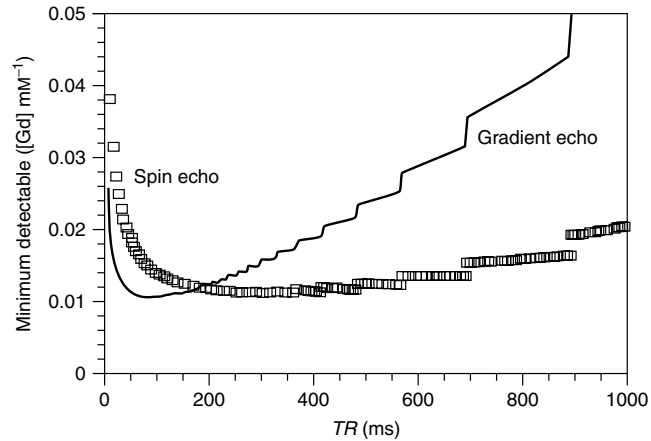


**Figure 2.12.** Mathematical modelling of image noise propagation predicts the minimum amount of Gd contrast agent that can be detected using a  $T_1$ -weighted sequence. By optimizing the repetition time,  $TR$ , in a spin echo or gradient echo sequence, its performance in white matter can be optimized. Theory indicates that, for a spin echo, the optimum  $TR = T_1/2$  (here it was assumed  $T_1 = 600$  ms). The gradient echo ( $FA = 50^\circ$ ), can achieve the same sensitivity, provided the correct  $TR$  is used. The examination time was fixed at 10 min. Reprinted from Tofts, P. S. 1996, Optimal detection of blood–brain barrier defects with Gd-DTPA MRI – the influences of delayed imaging and optimised repetition time, in *Magn. Reson. Imag.*, **14**, 373–380, Copyright 1996 with permission from Elsevier Science Ltd

This systematic error is most important in low-SNR images, where the mean value is increased by an amount dependent on the image noise. The maximum amount it can increase the mean by is  $0.66\sigma$  (at  $SNR = 0$ ), decreasing as SNR increases. The applications where this is most important are in  $T_2$  and diffusion measurements, where the decay of signal may be followed down into the noise (Miller and Joseph, 1993; Wheeler-Kingshott *et al.*, 2002), and perfusion, where the signal difference is comparable with the noise (Karlsen *et al.*, 1999). If image averaging is used to improve SNR, this should be carried out on the complex images, before formation of the magnitude. A correction can be made, provided the magnitude of the noise  $\sigma$  has been estimated. Although correction schemes can remove the bias (so that the mean value is correct), the distribution will still not be gaussian. *Noise estimation* can be made from the air values. Alternatively, it may be possible to use the difference between two images of the same uniform phantom.<sup>22</sup> In

<sup>22</sup> This subtraction technique may be invalid in phantoms (since loading is usually different from in subjects), and

high-SNR regions, the SD of the difference image equals  $\sqrt{2}$  times that in a single image (Edelstein *et al.*, 1986). The SD in a single image of a uniform object does not characterize the noise properly, because of the contribution of small amounts of nonuniformity from other sources. A more general approach, valid at any SNR, involves subtracting the squares of images. Sijbers *et al.* (1998) and others have discussed this problem (Gudbjartsson and Patz, 1995; Andersen, 1996).

A second method that has been proposed to deal with the problem of noise bias, when estimating  $T_2$ , is to form a ‘power image’, i.e. the square of the magnitude image (Miller and Joseph, 1993; McGibney and Smith, 1993). The images can then be fitted straightforwardly to obtain  $T_2$ . However the uncertainty in each power image is still different, and the points in the fit should be weighted to take account of this.

Multiaarray coil imaging techniques give images that are combined from several sources, often in a complex way (Bydder *et al.*, 2002). Although

impossible to carry out in subjects (because they would vary slightly between one image and the next).

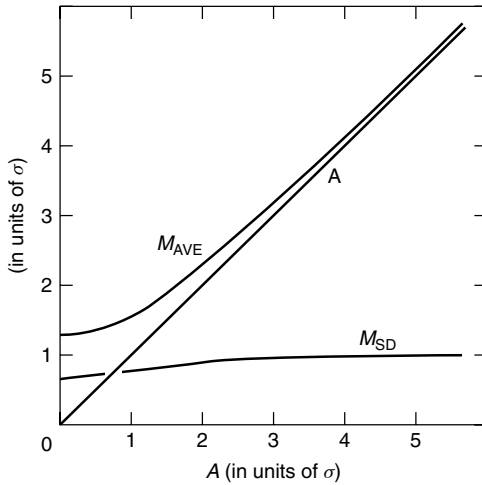


**Figure 2.13.** For a uniform region of an image with real amplitude  $A$  (measured in units of  $\sigma$ , the standard deviation of the noise in each dimension of the normal distribution), the average value  $M_{AVE}$  and the standard deviation  $M_{SD}$  in the magnitude ( $M$ ) image are shown, both expressed in units of  $\sigma$ . Thus at high SNR ( $A \gg \sigma$ ), the mean intensity in the magnitude image equals its value in a real image ( $M_{AVE} = A$ ), whilst at low SNR it exceeds the value in a real image, reaching an asymptotic value of  $1.253\sigma$  in the absence of any signal. At high SNR, the standard deviation equals that in a real image ( $M_{SD} = \sigma$ ), whilst in the absence of any signal it decreases to  $M_{SD} = 0.655\sigma$ . Reprinted with permission from Henkelman, R. M. 1985, Measurement of signal intensities in the presence of noise in MR images, in *Med. Phys.*, Copyright 1985

the resulting magnitude images will still have systematic bias at low SNR, the values in air will probably be different from those given above, and the mathematics given for a single coil are not necessarily valid.

### 2.1.8.2.3 Image Quantization Errors

Image intensity values are usually stored as integers, typically to 12-bit precision (i.e. 1 in 4096). The floating point values from the image reconstruction process are rounded to the nearest integer.<sup>23</sup> Typical signal values may be 500–1000;

<sup>23</sup> Rounding introduces a maximum error of 0.5, with rms value  $1/\sqrt{12} \approx 0.3$ .

thus the electrical noise will be a few units (for  $\text{SNR} = 100$ ), and quantization noise should be insignificant compared with electrical noise. If the floating point numbers are truncated (not rounded), a small amount of bias (0.5 image units) will be introduced. If histograms are to be produced from parameter maps, *image despiking*<sup>24</sup> should be carried out, to prevent the discrete image probability distribution from producing artefacts in the histograms (see Chapter 18).

### 2.1.9 Reciprocity Principle

The principle of reciprocity [see Equation (2.1)] states that the transmit field and the receive sensitivity at a particular point are closely related (Hoult, 1978; Hoult and Richards, 1976; Hoult, 2000). If a larger transmitter voltage is required to achieve a particular FA, because the coupling between the coil and the sample has been reduced for some reason, such as increased loading or the sample being more peripheral, then a smaller signal voltage will be received. The transmitter voltage and the signal voltage have a reciprocal relationship, in that as one goes up the other goes down, whilst the product stays constant. An example of the sample becoming more peripheral is given in Figure 2.14, and examples of changing loading are shown in Chapter 9 on spectroscopy (Figures 9.3 and 9.4). An alternative way to use the principle is to measure  $B_1$  and use this to determine the receive sensitivity (see Section 2.1.8.1).

The principle of reciprocity is the saving factor that allows the measurement of concentration of protons [either in water (i.e. PD) or metabolites (with spectroscopy)]; without this, it would be impossible to distinguish whether a change in signal voltage is caused by a change in proton concentration or a change in coil sensitivity.

More recently there has been discussion about whether this principle holds true at higher frequencies, and with novel coil designs (Tropp, 1993; Hoult, 2000; Fernandez-Seara *et al.*, 2001; Collins *et al.*, 2002). The transmission field is given by

<sup>24</sup> The integers are converted to floating point numbers and random noise with maximum magnitude 0.5 is added before calculation of the maps.

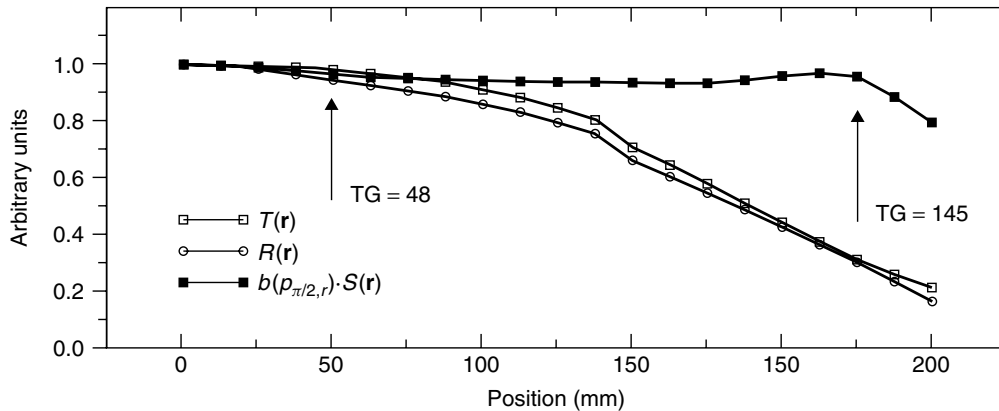


**Figure 2.14.** Reciprocity outside a head coil (using the data shown in Figure 2.6.).  $T(\mathbf{r})$  and  $R(\mathbf{r})$  show the drop off in  $B_1$  and receive sensitivity at ROIs increasingly distant from the coil.  $b(p/2, r)$  is proportional to the transmitter voltage needed to produce a  $90^\circ$  pulse at location  $\mathbf{r}$ .  $S(\mathbf{r})$  is the signal at location  $\mathbf{r}$ . The product of transmitter voltage and signal (upper data curve) is a constant, independent of location. This relationship holds as  $B_1$  and sensitivity drop by a factor of 3. TG is the transmitter output on a General Electric scanner (transmitter voltage  $\propto 10^{TG/200}$ ); the increase from TG = 48 to TG = 145 corresponds to a factor of 3.05. The dip above that value may be caused by transmitter nonlinearity. Reprinted with permission from Barker, G. J., Simmons, A., Arridge, S. R. and Tofts, P. S. 1998, A simple method for investigating the effects of non-uniformity of radiofrequency transmission and radiofrequency reception in MRI, in *Br. J. Radiol.* Copyright 1998 British Institute of Radiology

one of the circularly polarized components of  $B_1$  (typically  $B_1^+$ ), whilst the reception sensitivity is given by the other component ( $B_1^-$ ), and in general these are not equal (Sled and Pike, 1998; Collins and Smith, 2001). At 7T reciprocity failure has been observed (Figure 2.15). It is possible that measurements of proton concentration should be carried out at lower fields, or with particular types of RF coil, in order that reciprocity can be used.

### 2.1.10 Nonuniformity Correction

Early workers found that images were often visibly nonuniform. Surface coil images showed this particularly strongly, and the first corrections were made by imaging a *uniform object* and then dividing the human image by that of the uniform object (Axel *et al.*, 1987). If the transmit field is supplied by a separate, large coil, and the frequency is low enough to avoid any dielectric resonance effects, then this correction is valid. This approach was extended to head coil images (Condon *et al.*, 1987; Wicks *et al.*, 1993). Major sources of image

nonuniformity are the transmit field, the receive sensitivity, the receiver analogue filter that sets the bandwidth,<sup>25</sup> the restricted bandwidth of the receiver coil, gradient eddy currents and poor slice profile (causing cross-talk between adjacent slices, dependent on the slice number; Simmons *et al.*, 1994; Tofts *et al.*, 1994). On a modern system only the transmit and receive spatial variations are likely to be important (although if very accurate corrections are being made, this should be checked). It was recognized that the uniform object should be filled with oil, not water (see Section 3.4.1). If the sequence is relaxed then all tissues are equally affected by transmit nonuniformity, and correction by a uniform object is valid (provided the field is not too high). However as  $TR$  is shortened, the signal becomes dependent on the ratio of  $TR$  to  $T_1$ , the correction required is different for each tissue, and therefore it cannot be carried out using a uniform object. In addition, this approach becomes increasingly inaccurate at higher fields (since the

<sup>25</sup> This is no longer a problem on modern digital receiver systems.

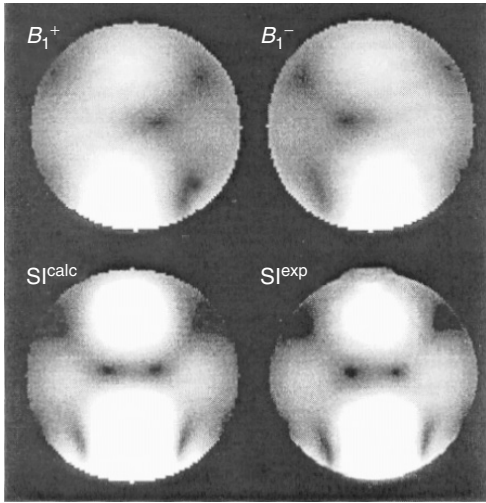


**Figure 2.15.** Reciprocity failure at 7 T. Theoretical  $B_1$  distributions in a 16 cm spherical NaCl solution phantom at 7 T, imaged with a 10 cm surface coil.  $B_{1+}$  is the circularly polarized transmit field,  $B_{1-}$  is the receive field.  $SI^{\text{calc}}$  and  $SI^{\text{exp}}$  are the theoretical (calculated) and measured (experimental) signal intensities for a gradient echo image; their similarity gives confidence in the modelling. Reprinted with permission from Collins, C. M., Yang, Q. X., Wang, J. H., Zhang, X., Liu, H., Michaeli, S., Zhu, X. H., Adriany, G., Vaughan, J. T., Anderson, P., Merkle, H., Ugurbil, K., Smith, M. B. and Chen, W. 2002. Different excitation and reception distributions with a single-loop transmit-receive surface coil near a head-sized spherical phantom at 300 MHz, in *Magn. Reson. Med.*, Copyright 2002 John Wiley & Sons Inc

RF distributions in the head and a uniform object differ), and scanning a uniform object is unlikely to have a major role in future quantitative work.

There have been many *software schemes* to correct visible image nonuniformity. These data-driven approaches have been called *retrospective* schemes, as opposed to *prospective* schemes which gather physical information about the instrument (Collewet *et al.*, 2002). For example the N3 method (Sled *et al.*, 1998) adjusts the postulated nonuniformity (expressed as a slowly varying function of position) to minimize the heterogeneity of corrected image intensity values. Such software methods are not, in the author's opinion, suitable

for quantitative work (although as a pre-processor for image registration they can be useful). The signal at a particular location may be reduced because of a reduction in PD, or because of a reduction in coil sensitivity, and without other information these two possibilities cannot be distinguished. The principle of reciprocity (see Section 2.1.9) and a measurement of the transmit field amplitude enable the receive sensitivity to be measured. Changes in PD and in sensitivity can then be distinguished. With the arrival of multiarray close-fitting head coils, RF nonuniformity will become worse, and the manufacturer's correction software may have to be disabled for proper quantification. There will be an increasing value in being able to use separate body-coil excitation.

Strategies for removing nonuniformity will have to make use of the reciprocity theorem to correct receive nonuniformity, if this is necessary. Many parameter maps (e.g.  $T_1$  and  $T_2$ ) are essentially the ratio of two images, and are therefore insensitive to receive nonuniformity. Receive sensitivity cancels out in the division.<sup>26</sup> PD and MRS measurements use the absolute signal value, measured relative to the value from a phantom, and are therefore very sensitive to changes in receive sensitivity, and corrections will be required. This implies using a receive coil which can also be used in transmit mode. Multiarray coils may thus exclude themselves, and it may be necessary to use the standard birdcage-type coils for such measurements. Transmit nonuniformity can be minimized by using the body coil, and measured if necessary (e.g. for MT studies) using the field mapping techniques summarized in Table 2.1. If there is already a requirement to map receive sensitivity (and therefore the  $B_1$  map for the receive coil will be available), it may be convenient to use this same coil for transmission. The saving in time (mapping one  $B_1$  field instead of two) has to be balanced against the increased nonuniformity (using the receive coil for transmission).

<sup>26</sup> This has been used as a convenient way to remove receive nonuniformity. The ratio of two spin echoes, at short and long echo time, can be used to calculate a  $T_2$  map, and receive nonuniformity is removed (Pope and Repin, 1988).

## 2.2 IMAGE ANALYSIS, STATISTICS AND CLASSIFICATION

### 2.2.1 Types of Image Analysis

There are three main ways of extracting relevant image intensities from a set of images that may cover many slices and many subjects.

#### 2.2.1.1 Region of Interest Analysis

The study is focussed on a particular part or parts of the brain, for example visible lesions or large volumes of normal-appearing white matter, where intensities are to be measured. One or several ROIs are drawn for each subject. Regions can be circular, oval, square, rectangular or irregular. Regions may be defined in a single slice or extend over several slices. They are often created using a semiautomatic technique (Plummer, 1992), which speeds up the process and improves the reproducibility. ROI size is a compromise between reducing noise (which favours large ROIs<sup>27</sup>) and reducing partial volume error (which favours small ROIs). The process of creating the ROIs takes some time to learn, and different observers will develop different approaches. Inter-observer<sup>28</sup> variation can be reduced by carefully defining the procedure to be used. This may include factors such as how the image is to be displayed, and a detailed description of what anatomical cues are to be used in positioning the ROI. Usually the intra-observer variation is lower, and many studies accept that a single observer should be used. Even for a single observer, the analysis should be repeated after a few days to ensure the reproducibility is reasonable. A formal measurement of reproducibility can be undertaken (see Section 3.1).

There may be multiple MR images or maps, for example conventional MRI (showing lesions in PD- or  $T_2$ -weighted images) and an MTR

map. The appearance of lesions may be different on the conventional MRI and the map. If the MTR values of lesions are to be measured and tested, the ROIs should ideally be defined on the conventional MR images, then transferred to the maps. If the ROIs were defined directly on the maps, the map intensity would influence where the ROI boundary was placed. ROIs tend to be attracted to locations of abnormal intensity (as a result of the process of their creation, where an observer tends to draw around distinct objects). Thus any conclusions about map values in the lesions would be biased, since these values were used to define which pixels would be included in the region. Large regions of most of the normal-appearing white or grey matter have been generated using  $T_1$  maps (Parkes and Tofts, 2002) or fractional diffusion anisotropy (Cercignani *et al.*, 2001).

To transfer ROIs between images in this way requires that the various images and maps are all spatially registered. Although the spatial resolution in each image is about 1–2 mm, subject movement may be larger than this. Registration can be achieved by using an interleaved sequence, which acquires information on the different parameters simultaneously (Barker *et al.*, 1996), by careful radiographic positioning and minimizing patient movement, or by software registration after data collection (see Chapter 15).

In studies of diffuse disease that affects large parts of the brain, instead of creating large regions to study this, two other approaches are available: histograms and voxel-based group mapping.

#### 2.2.1.2 Histogram Analysis

A solution to the problem of ROI placement, and possible bias arising from this process, is to test the whole brain. This is particularly appropriate for diseases where the biological effects are diffuse and widespread. To carry this out, the brain needs to be segmented (i.e. its outline defined); however this is a quite reproducible process, and histogram analysis is now very popular. Subregions of the brain, such as large tumours or the grey and white matter can also be studied (Dehmeshki

<sup>27</sup> The standard error of the mean in the ROI is the standard deviation in a single voxel divided by the square root of the number of voxels

<sup>28</sup> Inter-observer means ‘between observer’, i.e. the difference between measurements made by *different* observers on the same image data. Intra-observer means ‘within-observer’, i.e. the difference if the *same* observer repeats the measurement.

*et al.*, 2003). Histograms do have the disadvantage that localization information has been lost, and if disease only affects part of the region, sensitivity will be reduced by pooling data from the whole region. Histograms are discussed in detail in Chapter 18, and examples are given of their use in MT and diffusion.

### 2.2.1.3 Voxel-based Group Mapping – Beyond ROIs and Histograms

Analysis of group-mapped images provides a way of combining the ability of ROIs to be spatially specific (and thus sensitive) with the ability of histograms to be unbiased. In essence, a set of ROIs is automatically generated at locations across the whole brain, without any bias in where they are located. The image datasets are first spatially normalized to all lie in the same space. Appropriate statistical tests are then carried out on all the ROIs. The technique has been used in studies of child development (Paus *et al.*, 1999), aging (Good *et al.*, 2001), schizophrenia (Foong *et al.*, 2001; Shapleske *et al.*, 2002) and dementia [Scahill *et al.*, 2002; Figure 2.16 (Plate 1)]

The techniques have the following key steps (Paus *et al.*, 1999; Ashburner and Friston, 2000, 2001). Image datasets from all the subjects are spatially registered to the same stereotactic space (see Chapter 15). A nonuniformity correction can be made. The images are segmented into white matter, grey matter and CSF (lesions, if present, are not dealt with). Gaussian smoothing, with full-width half maximum typically 12 mm, is applied to reduce the effects of incomplete registration and residual inter-subject differences. A generalized linear model is then applied, enabling a variety of statistical tests to be carried out. In particular, group comparisons and correlations with an external parameter (such as disease severity or age) can be carried out. All locations are tested without prejudice, and the locations of significant group difference or correlation are found. Thus localized changes can be found without bias or loss of sensitivity. Corrections for multiple

comparisons are made using the theory of Gaussian random fields. The smoothing introduces correlations between adjacent voxels, so the overall effect is similar to placing a close-packed array of 12 mm independent ROIs on the image dataset, and analysing them all. Changes in grey or white matter volume can be found (this is often seen as an intensity change, as a result of the smoothing that has been applied). Changes in mapped parameters (MTR, perfusion, etc.) have also been studied.

There are several pitfalls in applying the technique (see e.g. Bookstein, 2001; Ashburner and Friston, 2001). Nonuniformity (which corresponds to a local change in voxel size) can cause the signal intensity to be altered. Nonetheless the technique is powerful in giving an unbiased test of all locations, and in drawing attention to locations where further ROI-based studies (on independent data) would be fruitful. Group mapping can be carried out using the SPM software package, which is available free of charge.<sup>29</sup> Examples are given in Figure 2.16 (Plate 1), and in Chapter 15 (Figure 15.15) and Chapter 16 (Figure 16.5 and 16.7).

## 2.2.2 Types of Statistical Analysis

Statistical analysis of the measurements is an increasingly complex procedure. Involvement with statisticians at an early stage in study design and analysis is advisable. Failure to be aware of statistical pitfalls can lead to embarrassing rejections by journal referees; sometimes re-analysis can address the problems, but sometimes data collection is fatally flawed. In this section the basic concepts relevant to statistical analysis of MR data are summarized; however for full treatment the reader should go to the books listed in Table 2.2. A short treatment of some relevant concepts is also given by Haacke *et al.* (1999) and Hendee and Ritenour (2002) contains a chapter on probability and statistics (see Table 1.1). Suitable software packages are SPSS (originally Statistical Package for the Social Sciences but now more general) and SAS. These have comprehensive manuals

<sup>29</sup> From the Functional Imaging Laboratory, University College London: [www.fil.ion.ucl.ac.uk](http://www.fil.ion.ucl.ac.uk)

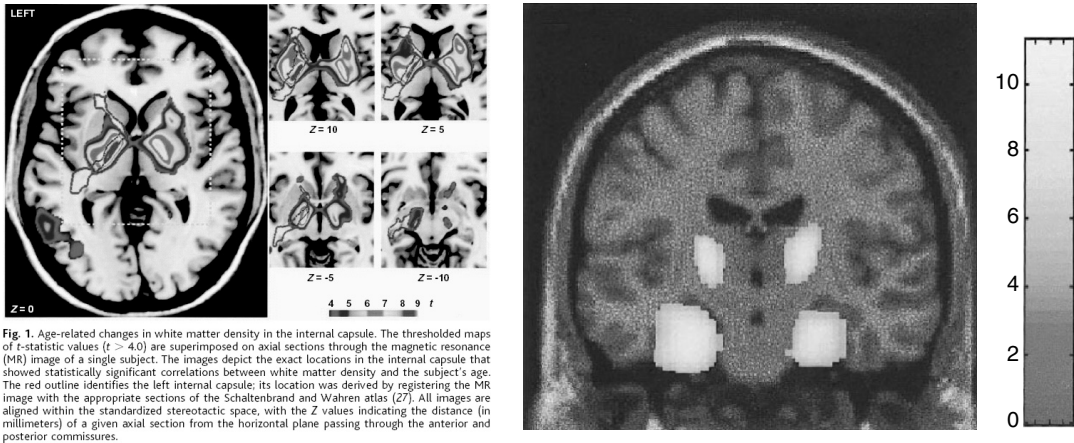
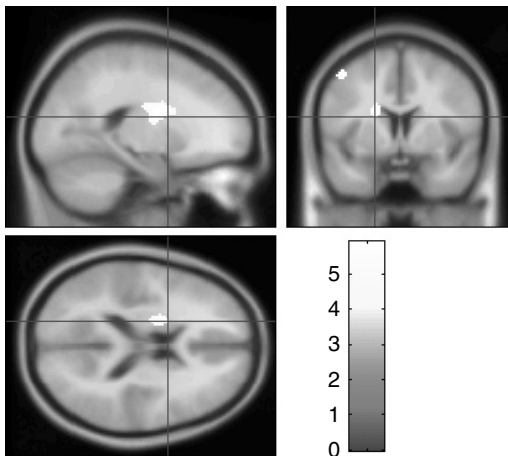


Fig. 1. Age-related changes in white matter density in the internal capsule. The thresholded maps of  $t$ -statistic values ( $t > 4.0$ ) are superimposed on axial sections through the magnetic resonance (MR) image of a single subject. The images depict the exact locations in the internal capsule that showed statistically significant correlations between white matter density and the subject's age. The red outline identifies the left internal capsule; its location was derived by registering the MR image with the appropriate sections of the Schaltenbrand and Wahren atlas (27). All images are aligned within the standardized stereotactic space, with the Z values indicating the distance (in millimeters) of a given axial section from the horizontal plane passing through the anterior and posterior commissures.



**Figure 2.16.** (Plate 1) Examples of voxel-based group mapping. (a) Child development shown by white matter correlations with age. (b) Aging shown by grey matter correlations with age (the bar shows the  $T$  score). (c) Gender difference in perfusion measured by arterial spin labelling. (a) Reprinted with permission from Paus, T., Zijdenbos, A., Worsley, K., Collins, D. L., Blumenthal, J., Giedd, J. N., Rapoport, J. L. and Evans, A. C., Structural maturation of neural pathways in children and adolescents: *in vivo* study, in *Science* 283 (5409), 1908–1911, Copyright 1999 American Association for the Advancement & Science. (b) Reprinted from Good, C. D., Johnsrude, I. S., Ashburner, J., Henson, R. N., Friston, K. J. and Frackowiak, R. S. 2001, A voxel-based morphometric study of ageing in 465 normal adult human brains, in *Neuroimage*. 14, 21–36, Copyright 2001 with permission from Elsevier Science Ltd. (c) Reprinted with permission from Parkes, L. M., Rashid, W., Chard, D. and Tofts, P. S. 2003, Normal cerebral perfusion measurements using arterial spin labelling; reproducibility, stability, age and gender effects. (*submitted*)

associated with them, and the software is often available through academic sources. The concepts discussed here come from three principle traditions – pure statistics, the physical sciences and psychology, – and this can be seen in the origins of the books in the Table 2.3.

**Good practice in study design and statistics:**

1. Talk to a statistician before and after collecting the data.
2. Collect interleaved normal and patient data.

**Table 2.2.** Statistics books, from backgrounds of medical statistics, physical sciences and psychology

Title	Authors	Date published	Number of pages	Description
<i>Statistical Methods in Medical Research</i>	Peter Armitage, J.N.S. Matthews, Geoffrey Berry	2001	832	Classic from statisticians, 4th edn
<i>Practical Statistics for Medical Research</i>	Douglas Altman	1990	624	From a respected statistician
<i>An Introduction to Medical Statistics</i>	Martin Bland	2000	422	Paperback; see also Bland's website: <a href="http://www.sghms.ac.uk/depts/phs/staff/jmb/">www.sghms.ac.uk/depts/phs/staff/jmb/</a>
<i>SPSS for Windows Made Simple</i>	Paul R. Kinnear, Colin D. Gray	2000	432	Paperback manual for SPSS software package
<i>An Introduction to Error Analysis: the Study of Uncertainties in Physical measurements</i>	John R. Taylor	1997	488	From a physical scientist, 2nd edn.
<i>Data Reduction and Error Analysis for the Physical Sciences</i>	Philip R. Bevington, D. Keith Robinson, Philip Bevington	2002	336	3rd edn
<i>Statistics for Experimenters: an Introduction to Design, Data Analysis, and Model Building</i>	George E.P. Box, William G. Hunter, J. Stuart Hunter	1978	653	Classic, still in print
<i>British Medical Journal Statistical Notes</i>	Martin Bland and Douglas Altman	1994–2002	46 short articles	From the BMJ website or <a href="http://www.sghms.ac.uk/depts/phs/staff/jmb/pbstnote.htm">www.sghms.ac.uk/depts/phs/staff/jmb/pbstnote.htm</a>
<i>Biostatistical Analysis</i>	Jerrold H. Zar	1998	663	Slightly different viewpoints from the medical- and physics-based books
<i>Biometry: the Principles and Practice of Statistics in Biological Research</i>	Robert R. Sokal, F. James Rohlf	1994	880	
<i>Psychometric Theory</i>	Jum Nunnally, Ira Bernstein	1994	736	Classic from psychologists
<i>Health Measurement Scales: a Practical Guide to Their Development and Use</i>	David L. Streiner, Geoffrey R. Norman	1995	240	Good on clinical scales, paperback

3. Control for age and gender during subject recruitment.
4. Inspect the data in scatter plots.
5. Model the data, including random and systematic error.
6. Adjust for age and gender during analysis.
7. Avoid if possible doing  $t$ -tests with many comparisons.
8. Be aware that correlations are hard to interpret.
9. Give confidence limits on group means and differences.

### 2.2.2.1 Group Comparisons $t$ -Tests

An investigation of new MR parameters in a disease may result in many data. To test their usefulness, it is tempting to carry out multiple  $t$ -tests, for example to see if any of the parameters differ between clinical groups. Correlation with clinical scores may also be carried out (see below). If 20 tests are carried out at the  $p = 0.05$  significance level, on average one test will come out positive by chance (this is known as a type I error). Thus the results of multiple comparisons must be treated with caution. The Bonferroni correction for multiple comparisons (Bland and Altman, 1995) allows for this by suggesting that the appropriate  $p$ -value is the value that would have been used for a single test (e.g.  $p = 0.05$ ), divided by the number of comparisons (e.g. 20). A much reduced  $p$ -value (e.g. 0.002) is then used, and the chance of a type I error is reduced (in this example to 0.04). The Bonferroni correction can be unnecessarily cautious, missing an effect which is present (i.e. a type II error). If the outcome variables being tested are correlated, then the reduction of the  $p$ -value by the number of tests is too extreme. Conversely, if several of the tests show significance (which does imply correlation between the tested variables), then the chances of this occurring by chance are much lower than the chance of just one occurring by chance.

A useful distinction can be made between two kinds of study. A so-called ‘fishing expedition’ looks at many parameters, tests them at  $p = 0.05$ ,

accepting that some type I errors will occur, and uses this to gain insight or guide further studies. A strict hypothesis-driven study sets up the hypothesis *before analysis*, makes only one test, and is thus able to control type I and type II errors better. Thus a fishing expedition might be used to set up a hypothesis-driven study, which must be carried out on separate data. Alternatively, the data could be divided into two parts, the first used for fishing, and the second for a strict test (although the power of the study would be reduced by the smaller sample sizes).

#### 2.2.2.1.1 Negative Results

A group comparison may turn out negative. There are two possible explanations: firstly, the genuine biological spread in each group may be too large to pick out a significant difference between them; secondly, the effect of measurement error may have broadened the spread in the groups beyond its genuine biological value, enough to obscure genuine biological difference. There are two courses of action: first, estimates of measurement error and within-group variance should be made (see Section 3.3). This enables the intraclass correlation coefficient (ICC) to be calculated; a good ICC means that the groups are genuinely indistinguishable; a poor ICC means that the failure to distinguish may be caused by poor instrumentation. Second, the confidence limits on the group means, and the minimum detectable group difference, should be reported. Other workers can then judge whether improved technique (i.e. reduced measurement error) might enable them to obtain a positive result.

#### 2.2.2.1.2 Positive Results

If a positive result is obtained, the confidence limits on group means and group difference should be given for other groups to estimate whether their measurement errors are low enough to repeat the positive observation. False-positive results can be obtained if there is another factor that differs between the groups. This could be the time of scanning (if one group is scanned before a change in measurement procedure, and the other after the

change), or uncontrolled age, gender or lifestyle differences.

#### 2.2.2.2 Correlation with Clinical Score

In many studies, MR parameters are tested for correlation with a clinical measure (in MS, often the Expanded Disability Status Scale EDSS), in an attempt to investigate or demonstrate their clinical utility (or lack of it). A parameter with a high correlation coefficient is thought to be a good candidate for a surrogate MR marker of the disease. In MS, low correlation coefficients  $r$  are reported (typically 0.3–0.6, sometimes 0.8; Dehmeshki *et al.*, 2001). Significance values,  $p$ , are also given. Correlation values are attenuated by the imperfect reliability (i.e. scatter) in the MR and clinical scores (thus even if the two measures were intrinsically perfectly correlated, the correlation plot would show scatter about the line describing this relationship). Correlation does not imply causality, only association, and the association may be weakened by the introduction of another factor (such as treatment). Thus a good correlation between an MR parameter and a clinical score does not necessarily imply the parameter is a good MR surrogate in a treatment trial; more evidence is needed of a direct relationship between the biological changes that happen in the disease and the MR parameter.

An alternative way to think of the linear regression implied in correlation is: how well can the MR parameter predict the current value of the clinical parameter? Thus a high correlation implies that the MR parameter provides a good estimate of the current clinical status (see Chapter 18 Figure 18.10). The fraction of the variance in the clinical score explained by the MR parameter is  $r^2$ , and this is a useful interpretation of  $r$ .

Age and gender correlations with the principle variables can cause problems; they should be included in the correlation as covariates (Chard *et al.*, 2002).

#### 2.2.2.3 Clinical Scores

Clinical status can be quantified using scores. For example in MS the EDSS scale is used to measure

disability. In tumours a grading system is used, based on histology of biopsy samples. In psychiatric illness, a battery of psychometric tests, including cognitive and emotional, are in use. Newly introduced MR parameters have often been judged by how well they correlate with existing clinical scores; intensive effort has gone into characterizing the performance of the MR parameter (for example using sensitivity, validity and reliability – see Chapter 12, Section 12.6). In turn it has been accepted that the same intensive study should go into the clinical scores, and in fact they do have some serious shortcomings. EDSS is nonlinear, mixes impairments of ambulation, fine motor skill and cognition, and has limited reproducibility (Hobart *et al.*, 2000). Tumour grading based on sampling tissue is vulnerable to missing high-grade tissue in a heterogeneous tumour, and multicentre studies show appreciable differences in grading between pathologists, which can limit how well MRS classifiers can work. The psychological tests are generally better, because there is a longer-standing tradition of test design in that field, although learning, floor and ceiling effects and tiredness are still important limitations.

Scores that are more appropriate are being designed. In MS the functional composite score (MSFC score) is increasingly popular (Fischer *et al.*, 1999; Cohen *et al.*, 2000). It consists of three components, which measure different aspects of impairment. Leg function and ambulation are measured by the timed 25-foot walk,<sup>30</sup> arm function by the nine-hole peg test, and cognition by the Paced Auditory Serial Addition Test. Correlations of MR parameters with these individual components may be superior, since they reflect different impairments which may occur at different times in the evolution of the disease, and originate from different locations in the CNS. There is still controversy over how reliable these measurements are, since there may be learning effects in the subjects. A correlation plot may show an approximately linear dependence of a MR parameter on EDSS, but the line will often not go through the normal point (normal MR value, EDSS = 0), possibly because

<sup>30</sup> Often replaced by the 10 m walk in Europe.

subclinical changes happen to the MR parameter before any clinical disability is apparent.

In view of these shortcomings in clinical scores, and the complex relationship between biological changes and the ensuing clinical changes, a failure of MR parameters to closely predict these scores is hardly surprising. A more realistic test may be to look at how well the MR correlates with the biology, and with scores of simple human functions.

2.2.2.4 Classification of Individual Subjects, and ROC Curves

If a measurement is performing well in separating two groups of subjects (see above), then its performance on individual subjects is worth investigating. In computer science methodology, the MR measurements may be seen as an example of a *classifier*. A classifier is a software tool for deciding which class a number of subjects belong to, based on measurements made on each subject. Classification in its simplest case only attempts to choose between two classes (binary classification). A linear discriminant is often constructed, and a threshold used to assign the class [see for example Dehmshki *et al.* (2002) and Chapter 18 on histograms, Figure 18.9]. Classification techniques have been used in spectroscopy to classify tumours into several types (Tate *et al.*, 1998). The choice of threshold in a classifier is crucial in balancing false-positive and false-negative errors, and ROC formalism is an ideal way to view and optimize this balance.

Receiver operating characteristic (ROC) curves (Armitage *et al.*, 2001) are often used in binary classification, and are also appropriate here (Altman and Bland 1994a; Zweig and Campbell, 1993; Huo *et al.*, 2002). They originate from studies to characterize screens used by radar operators, and specifically recognize that the number of objects depends on how a particular operator is making their decisions. A low threshold of abnormality, i.e. reporting all objects which could possibly be real, would result in a large number of positive decisions. The proportion of actual objects detected (i.e. true positives) would be large, but at the expense of many false positives (which are in fact noise on the screen). A higher threshold

**Table 2.3.** Decision matrix in ROC formalism; the test is to report whether an object is present or not; it could equally well be to determine whether a disease is present or not

	Object reported not to be present	Object reported to be present
Object absent	True negative (TN)	False positive (FP)
Object present	False negative (FN)	True positive (TP)

(only reporting objects judged to be certainly real) would result in fewer positive decisions, more missed objects (false negatives), and fewer false positives (Table 2.3). Thus the choice of decision threshold allows true positives to be traded off against false positives, and a particular threshold, corresponding to a particular point on the curve, can be chosen according to the relative cost and benefit of false positives and false negatives. Thus in a screening program, false negatives are expensive, since missing a tumour may result in death, and false positives are also costly (although less so), since they produce unnecessary worry in the subjects.

An ROC curve can be generated by asking the observer to give a score with each object reported, for example: 0, object absent (corresponding to a low threshold); 1, object possibly present; 2, may be present; 3, probably present; 4, almost certainly present; 5, certainly present (corresponding to a high threshold). The scores can also be defined by their anticipated probabilities (e.g. 0, <10 % of being present; 1, 10–30 % of being present, etc.). The probabilities need not be correct; they just allow the observer to behave consistently. Combinations scores are summed to give points in the ROC space corresponding to different thresholds<sup>31</sup> (Figure 2.17). ROC curves can be fitted to analytic functions, to obtain a measure that enables ROC

<sup>31</sup> Thus threshold 1 corresponds to objects detected with scores 1–5 (i.e. all objects), threshold 2 is object scores 2–5 (i.e. certainty of ‘probably’ or more), etc., and each threshold gives a point on the ROC curve.

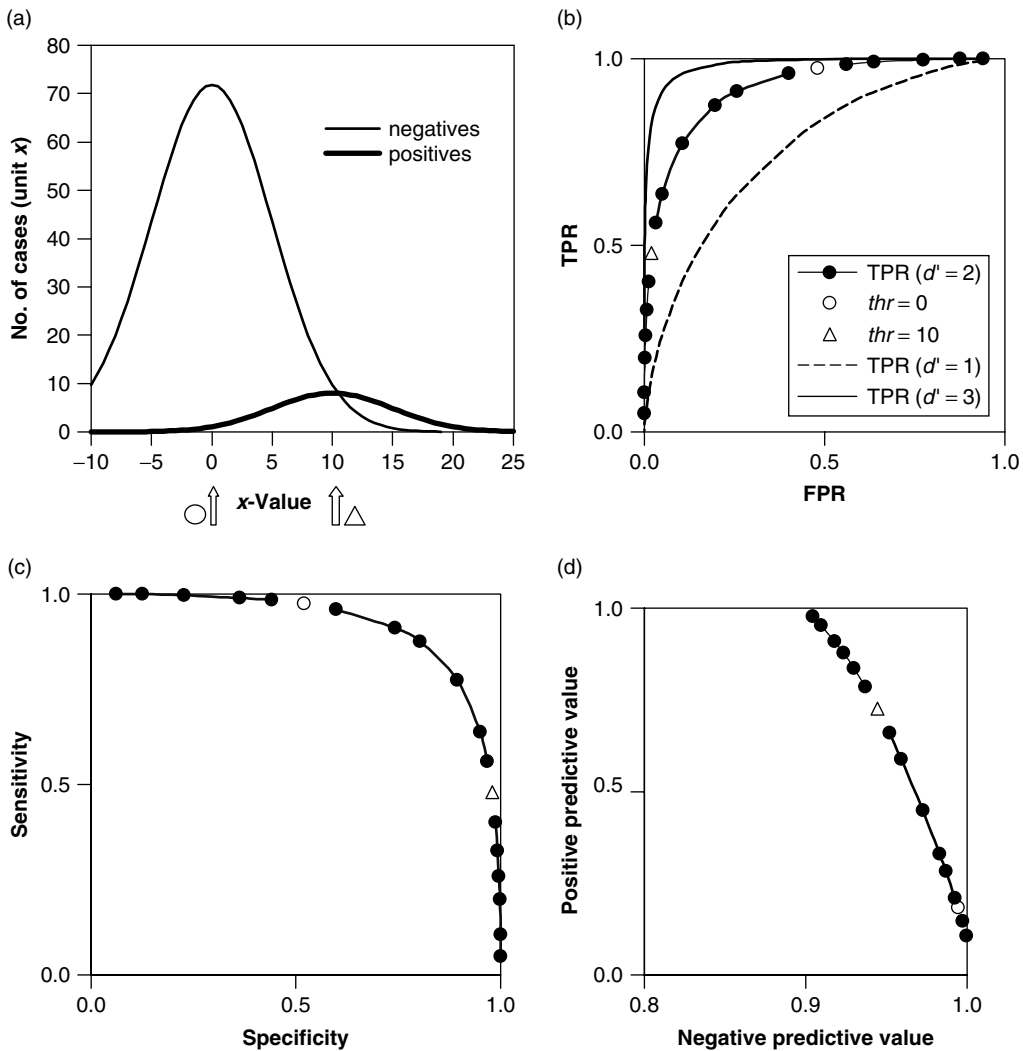


**Figure 2.17.** An ROC computer simulation. (a) negative (N) and positive (P) normal distributions. There are 1000 cases, a prevalence of 1 in 10 (so 100 positive cases). Mean values are  $x = 0$  and  $x = 10$ . Standard deviation is 5 for both groups [the expressions for the normal probability functions are given in Equation (2.10)]. (b) ROC curve (labelled  $d' = 2$ , meaning that the distributions are separated by 2 SD). Points from thresholds at the centre of each distribution are shown in parts (b), (c) and (d) ( $thr = 0$ , centre of negatives;  $thr = 10$ , centre of positives). (Cases to the right-hand side of the threshold are reported positive. Thus the part of the negative tail to the right of the threshold contributes false positives, which decrease with threshold value. Conversely, the part of the positive tail to the left of the threshold gives false negatives; as the threshold is increased these increase, reducing the true positive rate, TPR.) Curves for other separations ( $d' = 1$ , i.e. 5 units, and  $d' = 3$ , i.e. 15 units) are shown. The decision criterion to generate the N and P results is that an  $x$ -value greater than the threshold indicates that the sample comes from the P distribution. (c) Sensitivity vs specificity plot which is the left–right reflection of the Recursive. (d) Positive negative predictive values both depend on the threshold (and also on the prevalence)

curves to be compared, and to provide an element of smoothing (Constable *et al.*, 1995; Sorenson and Wang, 1996).

Radiologists use the terms *sensitivity*, *specificity*, *positive predictive value*, *negative predictive value*,

*accuracy* and *prevalence* in the context of how well a test performs (Altman and Bland, 1994b,c; Dalton *et al.*, 2002). These can be defined in terms of the number of true and false positive and negative reports (Table 2.4).

**Table 2.4.** Radiological terms summarizing the performance of a test; in this case the test is to find out whether subjects have a disease or not. Negative indicates that they do not, positive that they do. Sensitivity and specificity define the performance of the test (regardless of prevalence), whilst predictive value and accuracy depend on prevalence (i.e. what fraction of the sample has the disease). Thus the latter quantities are very different for an asymptomatic screened population and a symptomatic hospital population

Term	Formal definition	Formula	Comment	Dependent on prevalence?
Sensitivity	The probability of the test finding the disease amongst those who have the disease	$TP/(TP + FN)$	Sensitivity characterizes the false negatives	No
Specificity	The probability of the test finding no disease amongst those who do not have the disease	$TN/(TN + FP)$	Specificity characterizes the false positives	No
Positive predictive value	The fraction of people with a positive test result who do have the disease	$TP/(TP + FP)$	Fraction of <i>positive</i> reports that are correct	Yes
Negative predictive value	The fraction of people with a negative test result who do not have the disease	$TN/(TN + FN)$	Fraction of <i>negative</i> reports that are correct	Yes
Accuracy	The fraction of test results that are correct	$(TP + TN)/(TP + TN + FP + FN)$	Fraction of <i>all reports</i> that are correct	Yes
Prevalence	The fraction of the sample that has the disease	$(TP + FN)/(TP + TN + FP + FN)$	Distinguish from incidence <sup>a</sup>	–
True positive rate TPR	Fraction of positive cases that are detected	$TP/(TP + FN)$	Equals sensitivity. The fractional area under the positive curve that is to the right of the threshold	No
False positive rate FPR	Fraction of negative cases that are reported positive	$FP/(TN + FP)$	Equals $1 - \text{specificity}$ . The fractional area under the negative curve that is to the right of the threshold	No

<sup>a</sup> Thus the prevalence is the fraction of people that have a particular disease at any one time. The *incidence* is the number of *new cases* of disease that arise in a given period (usually one year) for a given size of population.

The false-positive rate, equal to the fraction of the negative distribution that is to the right of the threshold (see Figure 2.17), is known in statistics as the significance, the  $\alpha$ -value, p-value or the chance of a type I error. The false-negative rate, equal to the fraction of the positive distribution that is to the left of the threshold, is the  $\beta$ -value, q-value or the chance of a type II error (Armitage *et al.*, 2001; Haacke *et al.*, 1999).

### 2.2.2.5 Multiparametric Analysis

There is some evidence that multiparametric studies can increase the ability to characterize biological changes in tissue. Such measurements can improve image segmentation, and also have potential to give improved prediction of clinical outcome, particularly in MS and ischaemia (Confort-Gouny *et al.*, 1993; Mainero *et al.*, 2001; Bernarding *et al.*, 2000; van Waesberghe *et al.*, 1997; Iannucci *et al.*, 2001) and clinical examples in Chapter 11, e.g. Figure 11.13. Since each MR parameter is giving information about different aspects of the biology, this is hardly surprising. If several MR parameters all correlate with clinical scores, and do not correlate strongly with each other, then there is a case for measuring them all. A recent plea in the journal *Neurology*, on the subject of MRI techniques to monitor MS evolution (Filippi and Grossman, 2002); asked that:

- (1) metrics from magnetization transfer MRI, diffusion-weighted MRI and proton MRS should be implemented to obtain reliable *in vivo* quantification of MS pathology;
- (2) multiparametric MRI should be used in all possible clinical circumstances and trials;
- (3) reproducible quantitative MR measures should ideally be used for the assessment of patients and are essential for trials.

Diagnosis at an early stage of a disease with a long and variable course, and prediction of disease progression, on the basis of very early symptoms, can be viewed as a multiparametric problem where MRI and other data are available. Their combination can be optimized to provide the best prediction of future clinical status, measured according to various clinical scores,

according to various criteria such as sensitivity, specificity and predictive value (see Table 2.5)•. The effects of disease are similarly multidimensional, and need several scores to properly characterize them, for example in MS, see Barkhof *et al.* (1997), Fischer *et al.* (1999) and Tintore *et al.* (2000). To assemble multiparametric MR data, features can be extracted from histograms of each MR parameter, and from lesion values. Voxel-by-voxel analysis of images requires that image datasets have been spatially registered. Statistical techniques such as multiple linear discriminant analysis and cluster analysis are appropriate (Tintore *et al.*, 2001).

## 2.2.3 The Future of Image Analysis

Multiparametric studies, better use of appropriate clinical scores and more subtle use of localized analysis will all increase the performance of MR parameters in characterizing disease. In a recent multiparametric study in MS, Oh *et al.* (2002)<sup>32</sup> has shown that correlations with clinical scores can be improved by (i) using multiparametric MR scores (combined using linear discriminant analysis) in place of a single score, (ii) using localized measurements in the corpus callosum<sup>33</sup> instead of in the whole brain and (iii) using psychometric scores such as the nine-hole peg test in place of EDSS.

Radiological reporting may become increasingly ROC-oriented, to take account of the differing characteristics of the radiologists. Three-dimensional volume datasets, with typical slice thickness of 1–2 mm, are too large to be reported manually. Sometimes the thin slices are merged into thicker slices for reporting; however this overwhelming amount of data will drive the progress of automated systems for segmentation and analysis. Pre-processors can carry out the computer-intensive work that is boring for a human reporter

<sup>32</sup> Submitted for publication as ‘The relationship of regional proton magnetic resonance spectroscopy, diffusion tensor and magnetization transfer imaging metrics to clinical disability in multiple sclerosis’, by J. Oh *et al.*

<sup>33</sup> The corpus callosum is a broad band of nerve fibres that joins the two hemispheres of the brain.

and present ambivalent results for final judgement by the experienced human viewer.

### 2.2.4 Acknowledgements

Petra Schmalbrock, Lizann Bolinger and Maria Fernandez-Seara gave insight into field mapping. Gareth Barker advised on the use of hard pulses in  $B_1$  field mapping. Martin King, Hilary Watt, Declan Chard, Caroline Selai and Anwar Padhani contributed helpful material and discussion on statistics.

### REFERENCES

- Alecci, M., Collins, C. M., Smith, M. B. and Jezzard, P. 2001, Radio frequency magnetic field mapping of a 3 Tesla birdcage coil: experimental and theoretical dependence on sample properties, *Magn. Reson. Med.*, **46**, 379–385.
- Alsop, D., Watkins, R. D., Greenman, R., Schenk, J. and Lenkinski, R. 2001, in vivo mapping of  $B_1$  uniformity produced by a whole body 3 T coil, *Proc. Intl. Soc. Mag. Reson. Med.*, **9**, 1094.
- Altman, D. G. and Bland, J. M. 1994a, Diagnostic tests 3: receiver operating characteristic plots, *Br. Med. J.*, **309**(6948), 188.
- Altman, D. G. and Bland, J. M. 1994b, Diagnostic tests. 1: Sensitivity and specificity, *Br. Med. J.*, **308**(6943), 1552.
- Altman, D. G. and Bland, J. M. 1994c, Diagnostic tests 2: Predictive values, *Br. Med. J.*, **309**(6947), 102.
- Andersen, A. H. 1996, On the Rician distribution of noisy MRI data, *Magn. Reson. Med.*, **36**, 331–333.
- Akoka, S., Franconi, F., Seguin, F. and Le Pape, A. 1993, Radiofrequency map of an NMR coil by imaging, *Magn. Reson. Imag.*, **11**, 437–441.

and present ambivalent results for final judgement by the experienced human viewer.

### 2.2.4 Acknowledgements

Petra Schmalbrock, Lizann Bolinger and Maria Fernandez-Seara gave insight into field mapping. Gareth Barker advised on the use of hard pulses in  $B_1$  field mapping. Martin King, Hilary Watt, Declan Chard, Caroline Selai and Anwar Padhani contributed helpful material and discussion on statistics.

### REFERENCES

- Alecci, M., Collins, C. M., Smith, M. B. and Jezzard, P. 2001, Radio frequency magnetic field mapping of a 3 Tesla birdcage coil: experimental and theoretical dependence on sample properties, *Magn. Reson. Med.*, **46**, 379–385.
- Alsop, D., Watkins, R. D., Greenman, R., Schenk, J. and Lenkinski, R. 2001, in vivo mapping of  $B_1$  uniformity produced by a whole body 3 T coil, *Proc. Intl. Soc. Mag. Reson. Med.*, **9**, 1094.
- Altman, D. G. and Bland, J. M. 1994a, Diagnostic tests 3: receiver operating characteristic plots, *Br. Med. J.*, **309**(6948), 188.
- Altman, D. G. and Bland, J. M. 1994b, Diagnostic tests. 1: Sensitivity and specificity, *Br. Med. J.*, **308**(6943), 1552.
- Altman, D. G. and Bland, J. M. 1994c, Diagnostic tests 2: Predictive values, *Br. Med. J.*, **309**(6947), 102.
- Andersen, A. H. 1996, On the Rician distribution of noisy MRI data, *Magn. Reson. Med.*, **36**, 331–333.
- Akoka, S., Franconi, F., Seguin, F. and Le Pape, A. 1993, Radiofrequency map of an NMR coil by imaging, *Magn. Reson. Imag.*, **11**, 437–441.

- Armitage, P., Matthews, J. N. S. and Berry, G. 2001, *Statistical Methods in Medical Research*. Blackwell, Oxford.
- Ashburner, J. and Friston, K. J. 2000, Voxel-based morphometry – the methods, *Neuroimage*, **11**(Pt 1), 805–821.
- Ashburner, J. and Friston, K. J. 2001, Why voxel-based morphometry should be used, *Neuroimage*, **14**, 1238–1243.
- Axel, L., Costantini, J. and Listerud, J. 1987, Intensity correction in surface-coil MR imaging, *Am. J. Roentgenol.*, **148**, 418–420.
- Barker, G. J. and Tofts, P. S. 1992, Semiautomated quality assurance for quantitative magnetic resonance imaging, *Magn. Reson. Imag.*, **10**, 585–595.
- Barker, P. B., Soher, B. J., Blackband, S. J., Chatham, J. C., Mathews, V. P. and Bryan, R. N. 1993, Quantitation of proton NMR spectra of the human brain using tissue water as an internal concentration reference, *NMR Biomed.*, **6**, 89–94.
- Barker, G. J., Tofts, P. S. and Gass, A. 1996, An interleaved sequence for accurate and reproducible clinical measurement of magnetization transfer ratio, *Magn. Reson. Imag.*, **14**, 403–411.
- Barker, G. J., Simmons, A., Arridge, S. R. and Tofts, P. S. 1998, A simple method for investigating the effects of non-uniformity of radiofrequency transmission and radiofrequency reception in MRI, *Br. J. Radiol.*, **71**(841), 59–67.
- Barkhof, F., Filippi, M., Miller, D. H., Scheltens, P., Campi, A., Polman, C. H., Comi, G., Ader, H. J., Losseff, N. and Valk, J. 1997, Comparison of MRI criteria at first presentation to predict conversion to clinically definite multiple sclerosis, *Brain*, **120**(Pt 11), 2059–2069.
- Bernarding, J., Braun, J., Hohmann, J., Mansmann, U., Hoehn-Berlage, M., Stapf, C., Wolf, K. J. and Tolxdorff, T. 2000, Histogram-based characterization of healthy and ischemic brain tissues using multiparametric MR imaging including apparent diffusion coefficient maps and relaxometry, *Magn. Reson. Med.*, **43**, 52–61.
- Bland, J. M. and Altman, D. G. 1995, Multiple significance tests: the Bonferroni method, *Br. Med. J.*, **310**(6973), 170.
- Bookstein, F. L. 2001, Voxel-based morphometry should not be used with imperfectly registered images, *Neuroimage*, **14**, 1454–1462.
- Bydder, M., Larkman, D. J. and Hajnal, J. V. 2002, Generalized SMASH imaging, *Magn. Reson. Med.*, **47**, 160–170. Claverdon Press, Oxford.
- Callaghan, P. T. 1993, *Principles of Nuclear Magnetic Resonance Microscopy*. Claverdon Press, Oxford.
- Carlson, J. W. and Kramer, D. M. 1990, Rapid radiofrequency calibration in MRI, *Magn. Reson. Med.*, **15**, 438–445.
- Cercignani, M., Inglese, M., Siger-Zajdel, M. and Filippi, M. 2001, Segmenting brain white matter, gray matter and cerebro-spinal fluid using diffusion tensor-MRI derived indices, *Magn. Reson. Imag.*, **19**, 1167–1172.
- Chard, D. T., Griffin, C. M., Parker, G. J., Kapoor, R., Thompson, A. J. and Miller, D. H. 2002, Brain atrophy in clinically early relapsing-remitting multiple sclerosis, *Brain*, **125**(Pt 2), 327–337.
- Clare, S. and Jezzard, P. 2001, Rapid T(1) mapping using multislice echo planar imaging, *Magn. Reson. Med.*, **45**, 630–634.
- Cohen, J. A., Fischer, J. S., Bolibrush, D. M., Jak, A. J., Kniker, J. E., Mertz, L. A., Skaramagas, T. T. and Cutter, G. R. 2000, Intrarater and interrater reliability of the MS functional composite outcome measure, *Neurology*, **54**, 802–806.
- Collewet, G., Davenel, A., Toussaint, C. and Akoka, S. 2002, Correction of intensity nonuniformity in spin-echo T(1)-weighted images, *Magn. Reson. Imag.*, **20**, 365–373.
- Collins, C. M. and Smith, M. B. 2001, Signal-to-noise ratio and absorbed power as functions of main magnetic field strength, and definition of “90 degrees” RF pulse for the head in the birdcage coil, *Magn. Reson. Med.*, **45**, 684–691.
- Collins, C. M., Yang, Q. X., Wang, J. H., Zhang, X., Liu, H., Michaeli, S., Zhu, X. H., Adriany, G., Vaughan, J. T., Anderson, P., Merkle, H., Ugurbil, K., Smith, M. B. and Chen, W. 2002, Different excitation and reception distributions with a single-loop transmit-receive surface coil near a head-sized spherical phantom at 300 MHz, *Magn. Reson. Med.*, **47**, 1026–1028.
- Condon, B. R., Patterson, J., Wyper, D., Jenkins, A. and Hadley, D. M. 1987, Image non-uniformity in magnetic resonance imaging: its magnitude and methods for its correction, *Br. J. Radiol.*, **60**(709), 83–87.
- Confort-Gouny, S., Vion-Dury, J., Nicoli, F., Dano, P., Donnet, A., Grazziani, N., Gastaut, J. L., Grisoli, F. and Cozzone, P. J. 1993, A multiparametric data analysis showing the potential of localized proton MR spectroscopy of the brain in the metabolic characterization of neurological diseases, *J. Neurol. Sci.*, **118**, 123–133.
- Constable, R. T., Skudlarski, P. and Gore, J. C. 1995, An ROC approach for evaluating functional brain MR

- imaging and postprocessing protocols, *Magn. Reson. Med.*, **34**, 57–64.
- Counsell, C. J. R. 1993, Stimulated echoes and spin echoes. Simultaneous determination of  $T_2$ , diffusion coefficient and RF homogeneity, *J. Magn. Reson. B*, **101**, 28–34.
- Dalton, C. M., Brex, P. A., Miszkil, K. A., Hickman, S. J., MacManus, D. G., Plant, G. T., Thompson, A. J. and Miller, D. H. 2002, Application of the new McDonald criteria to patients with clinically isolated syndromes suggestive of multiple sclerosis, *Ann. Neurol.*, **52**, 47–53.
- Dehmeshki, J., Ruto, A. C., Arridge, S., Silver, N. C., Miller, D. H. and Tofts, P. S. 2001, Analysis of MTR histograms in multiple sclerosis using principal components and multiple discriminant analysis, *Magn. Reson. Med.*, **46**, 600–609.
- Dehmeshki, J., Barker, G. J. and Tofts, P. S. 2002, Classification of disease subgroup and correlation with disease severity using magnetic resonance imaging whole-brain histograms: application to magnetization transfer ratios and multiple sclerosis, *IEEE Trans. Med. Imag.*, **21**, 320–331.
- Dehmeshki, J., Chard, D. T., Leary, S., Watt, H. C., Silver, N. C., Tofts, P. S., Thompson, A. J. and Miller, D. H. 2003, The normal appearing grey matter in primary progressive multiple sclerosis; a magnetisation transfer study, *J. Neurol.*, **250**, 67–74.
- Deichmann, R., Good, C. D. and Turner, R. 2002, RF inhomogeneity compensation in structural brain imaging, *Magn. Reson. Med.*, **47**, 398–402.
- Edelstein, W. A., Bottomley, P. A. and Pfeifer, L. M. 1984, A signal-to-noise calibration procedure for NMR imaging systems, *Med. Phys.*, **11**, 180–185.
- Edelstein, W. A., Glover, G. H., Hardy, C. J. and Redington, R. W. 1986, The intrinsic signal-to-noise ratio in NMR imaging, *Magn. Reson. Med.*, **3**, 604–618.
- Fakri-Bouchet, L., Lapray, C. and Briguet, A. 1998, Measurements of the radiofrequency field in magnetic resonance coils, *Meas. Sci. Technol.*, **9**, 1641–1646.
- Fernandez-Seara, M. A., Song, H. K. and Wehrli, F. W. 2001, Trabecular bone volume fraction mapping by low-resolution MRI, *Magn. Reson. Med.*, **46**, 103–113.
- Filippi, M. and Grossman, R. I. 2002, MRI techniques to monitor MS evolution: the present and the future, *Neurology.*, **58**, 1147–1153.
- Fischer, J. S., Rudick, R. A., Cutter, G. R. and Ringold, S. C. 1999, The Multiple Sclerosis Functional Composite Measure (MSFC): an integrated approach to MS clinical outcome assessment. National MS Society Clinical Outcomes Assessment Task Force, *Mult. Scler.*, **5**, 244–250.
- Foong, J., Symms, M. R., Barker, G. J., Maier, M., Woermann, F. G., Miller, D. H. and Ron, M. A. 2001, Neuropathological abnormalities in schizophrenia: evidence from magnetization transfer imaging, *Brain*, **124**(Pt 5), 882–892.
- Good, C. D., Johnsrude, I. S., Ashburner, J., Henson, R. N., Friston, K. J. and Frackowiak, R. S. 2001, A voxel-based morphometric study of ageing in 465 normal adult human brains, *Neuroimage*, **14**(Pt 1), 21–36.
- Gudbjartsson, H. and Patz, S. 1995, The Rician distribution of noisy MRI data, *Magn. Reson. Med.*, **34**, 910–914.
- Haacke, E. M., Brown, R. W., Thompson, M. R. and Venkatesan, R. 1999, *Magnetic Resonance Imaging. Physical Principles and Sequence Design*. Wiley-Liss, New York.
- Hendee, W. R. and Ritenour, E. R. 2002, *Medical Imaging Physics*, 4th edn., Wiley-Liss, New York.
- Henkelman, R. M. 1985, Measurement of signal intensities in the presence of noise in MR images, *Med. Phys.*, **12**, 232–233.
- Henkelman, R. M. 1986, Erratum: measurement of signal intensities in the presence of noise [*Med. Phys.* **12**, 232 (1985)], *Med. Phys.*, **13**, 544.
- Hobart, J., Freeman, J. and Thompson, A. 2000, Kurtzke scales revisited: the application of psychometric methods to clinical intuition, *Brain*, **123**(Pt 5), 1027–1040.
- Hornak, J. P., Szumowski, J. and Bryant, R. G. 1988, Magnetic field mapping, *Magn. Reson. Med.*, **6**, 158–163.
- Hoult, D. I. 1978, The NMR receiver: a description and analysis of design, *Progr. NMR Spectrosc.*, **12**, 41–77.
- Hoult, D. I. 2000, The principle of reciprocity in signal strength calculations – a mathematical guide., *Conc. Magn. Reson.*, **12**, 173–187.
- Hoult, D. I. and Richards, R. E. 1976, The signal-to-noise ratio of the nuclear magnetic resonance experiment, *J. Magn. Reson.*, **24**, 71–85.
- Hua, J. and Hurst, G. C. 1995, Analysis of on- and off-resonance magnetization transfer techniques, *J. Magn. Reson. Imag.*, **5**, 113–120.
- Huo, Z., Giger, M. L., Vyborny, C. J. and Metz, C. E. 2002, Breast cancer: effectiveness of computer-aided diagnosis observer study with independent database of mammograms, *Radiology*, **224**, 560–568.

- Hutton, C., Bork, A., Josephs, O., Deichmann, R., Ashburner, J. and Turner, R. 2002, Image distortion correction in fMRI: a quantitative evaluation, *Neuroimage*, **16**, 217–240.
- Iannucci, G., Rovaris, M., Giacomotti, L., Comi, G. and Filippi, M. 2001, Correlation of multiple sclerosis measures derived from  $T_2$ -weighted,  $T_1$ -weighted, magnetization transfer, and diffusion tensor MR imaging, *Am. J. Neuroradiol.*, **22**, 1462–1467.
- Ibrahim, T. S., Lee, R., Baertlein, B. A., Abduljalil, A. M., Zhu, H. and Robitaille, P. M. 2001, Effect of RF coil excitation on field inhomogeneity at ultra high fields: a field optimized TEM resonator, *Magn. Reson. Imag.*, **19**, 1339–1347.
- Insko, E. K. and Bolinger, L. 1993, Mapping the radiofrequency field, *J. Magn. Reson. Ser. A*, **103**, 82–85.
- Jezzard, P. 2002, Physical basis of spatial distortions in Magnetic Resonance Images, in *Handbook of Medical Imaging*, Bankman, Is. (ed.). Academic Press, London.
- Jezzard, P. and Balaban, R. S. 1995, Correction for geometric distortion in echo planar images from  $B_0$  field variations, *Magn. Reson. Med.*, **34**, 65–73.
- Joseph, P. M., Axel, L. and O'Donnell, M. 1984, Potential problems with selective pulses in NMR imaging systems, *Med. Phys.*, **11**, 772–777.
- Karlsen, O. T., Verhagen, R. and Bovee, W. M. 1999, Parameter estimation from Rician-distributed data sets using a maximum likelihood estimator: application to  $T_1$  and perfusion measurements, *Magn. Reson. Med.*, **41**, 614–623.
- Lemieux, L. and Barker, G. J. 1998, Measurement of small inter-scan fluctuations in voxel dimensions in magnetic resonance images using registration, *Med. Phys.*, **25**, 1049–1054.
- Mainero, C., De Stefano, N., Iannucci, G., Sormani, M. P., Guidi, L., Federico, A., Bartolozzi, M. L., Comi, G. and Filippi, M. 2001, Correlates of MS disability assessed in vivo using aggregates of MR quantities, *Neurology*, **56**, 1331–1334.
- McGibney, G. and Smith, M. R. 1993, An unbiased signal-to-noise ratio measure for magnetic resonance images, *Med. Phys.*, **20**, 1077–1078.
- Meyer, M. E., Yu, O., Eclancher, B., Grucker, D. and Chambron, J. 1995, NMR relaxation rates and blood oxygenation level, *Magn. Reson. Med.*, **34**, 234–241.
- Miller, A. J. and Joseph, P. M. 1993, The use of power images to perform quantitative analysis on low SNR MR images, *Magn. Reson. Imag.*, **11**, 1051–1056.
- Moerland, M. A., Beersma, R., Bhagwandien, R., Wijrdeman, H. K. and Bakker, C. J. 1995, Analysis and correction of geometric distortions in 1.5 T magnetic resonance images for use in radiotherapy treatment planning, *Phys. Med. Biol.*, **40**, 1651–1654.
- Oh, C. H., Hilal, S. K., Cho, Z. H. and Mun, I. K. 1990, Radio frequency field intensity mapping using a composite spin-echo sequence, *Magn. Reson. Imag.*, **8**, 21–25.
- Oh, J., Pelletier, D., Henry, R. G., Majumdar, S., Genain, C. and Nelson, S. J. 2002, Regional proton magnetic resonance spectroscopy, diffusion tensor and magnetisation transfer imaging metrics related to clinical disability in relapsing remitting and secondary progressive multiple sclerosis, *Proc. Int. Soc. Mag. Reson. Med.*, **10**, 591.
- Pan, J. W., Twieg, D. B. and Hetherington, H. P. 1998, Quantitative spectroscopic imaging of the human brain, *Magn. Reson. Med.*, **40**, 363–369.
- Parker, G. J., Barker, G. J. and Tofts, P. S. 2001, Accurate multislice gradient echo T(1) measurement in the presence of non-ideal RF pulse shape and RF field nonuniformity, *Magn. Reson. Med.*, **45**, 838–845.
- Parkes, L. M. and Tofts, P. S. 2002, Improved accuracy of human cerebral blood perfusion measurements using arterial spin labeling: accounting for capillary water permeability, *Magn. Reson. Med.*, **48**, 27–41.
- Parkes, L. M., Rashid, W., Chard, D. and Tofts, P. S. 2003, Normal cerebral perfusion measurements using arterial spin labelling: reproducibility, stability, age and gender effects (submitted).
- Pauly, J., Le Roux, P., Nishimura, D. and Macovski, A. 1991, Parameter relations for the Shinnar–Le Roux selective excitation pulse design algorithm., *IEEE Trans. Med. Imag.*, **10**, 53–65.
- Paus, T., Zijdenbos, A., Worsley, K., Collins, D. L., Blumenthal, J., Giedd, J. N., Rapoport, J. L. and Evans, A. C. 1999, Structural maturation of neural pathways in children and adolescents: *in vivo* study, *Science*, **283**(5409), 1908–1911.
- Perman, W. H., Bernstein, M. A. and Sandstrom, J. C. 1989, A method for correctly setting the rf flip angle, *Magn. Reson. Med.*, **9**, 16–24.
- Plummer, D. L. 1992, DispImage: a display and analysis tool for medical images, *Riv. Neuroradiol.*, **5**, 489–495.
- Pope, J. M. and Repin, N. 1988, A simple approach to  $T_2$  imaging in MRI, *Magn. Reson. Imag.*, **6**, 641–646.
- Scahill, R. I., Schott, J. M., Stevens, J. M., Rossor, M. N. and Fox, N. C. 2002, Mapping the evolution of regional atrophy in Alzheimer's disease: unbiased analysis of fluid-registered serial MRI, *Proc. Natl. Acad. Sci. U. S. A.*, **99**, 4703–4707.

- Shapleske, J., Rossell, S. L., Chitnis, X. A., Suckling, J., Simmons, A., Bullmore, E. T., Woodruff, P. W. and David, A. S. 2002, A computational morphometric MRI study of schizophrenia: effects of hallucinations, *Cereb. Cortex*, **12**, 1331–1341.
- Sijbers, J., den Dekker, A. J., Van Audekerke, J., Verhoye, M. and Van Dyck, D. 1998, Estimation of the noise in magnitude MR images, *Magn. Reson. Imag.*, **16**, 87–90.
- Simmons, A., Tofts, P. S., Barker, G. J. and Arridge, S. R. 1994, Sources of intensity nonuniformity in spin echo images at 1.5 T, *Magn. Reson. Med.*, **32**, 121–128.
- Skinner, T. E. and Glover, G. H. 1997, An extended two-point Dixon algorithm for calculating separate water, fat, and  $B_0$  images, *Magn. Reson. Med.*, **37**, 628–630.
- Sled, J. G. and Pike, G. B. 1998, Standing-wave and RF penetration artifacts caused by elliptic geometry: an electrodynamic analysis of MRI, *IEEE Trans. Med. Imag.*, **17**, 653–662.
- Sled, J. G. and Pike, G. B. 2000, Correction for  $B(1)$  and  $B(0)$  variations in quantitative  $T(2)$  measurements using MRI, *Magn. Reson. Med.*, **43**, 589–593.
- Sled, J. G., Zijdenbos, A. P. and Evans, A. C. 1998, A nonparametric method for automatic correction of intensity nonuniformity in MRI data, *IEEE Trans. Med. Imag.*, **17**, 87–97.
- Sorenson, J. A. and Wang, X. 1996, ROC methods for evaluation of fMRI techniques, *Magn. Reson. Med.*, **36**, 737–744.
- Stollberger, R. and Wach, P. 1996, Imaging of the active  $B_1$  field *in vivo*, *Magn. Reson. Med.*, **35**, 246–251.
- Stollberger, R. and Wach, P. 1997, Imaging of the active  $B_1$  field *in vivo* – erratum, *Magn. Reson. Med.*, **38**, 336.
- Stollberger, R., Wach, P., McKinnon, G., Justich, E. and Ebner, F. 1988, RF field mapping *in vivo*, *Proceedings of the Society of Magnetic Resonance Medicine*, works-in-progress volume, 106.
- Talagala, S. L. and Gillen, J. 1991, Experimental determination of three-dimensional RF magnetic field distribution of NMR coils, *J. Magn. Reson.*, **94**, 493–500.
- Tate, A. R., Griffiths, J. R., Martinez-Perez, I., Moreno, A., Barba, I., Cabanas, M. E., Watson, D., Alonso, J., Bartumeus, F., Isamat, F., Ferrer, I., Vila, F., Ferrer, E., Capdevila, A. and Arus, C. 1998, Towards a method for automated classification of 1H MRS spectra from brain tumours, *NMR Biomed.*, **11**, 177–191.
- Tintore, M., Rovira, A., Martinez, M. J., Rio, J., Diaz-Villoslada, P., Brieua, L., Borrás, C., Grive, E., Capellades, J. and Montalban, X. 2000, Isolated demyelinating syndromes: comparison of different MR imaging criteria to predict conversion to clinically definite multiple sclerosis, *Am. J. Neuroradiol.*, **21**, 702–706.
- Tintore, M., Rovira, A., Brieua, L., Grive, E., Jardi, R., Borrás, C. and Montalban, X. 2001, Isolated demyelinating syndromes: comparison of CSF oligoclonal bands and different MR imaging criteria to predict conversion to CDMS, *Mult. Scler.*, **7**, 359–363.
- Tofts, P. S. 1996, Optimal detection of blood–brain barrier defects with Gd-DTPA MRI—the influences of delayed imaging and optimised repetition time, *Magn. Reson. Imag.*, **14**, 373–380.
- Tofts, P. S., Kermode, A. G., MacManus, D. G. and Robinson, W. H. 1990, Nasal orientation device to control head movement during CT and MR studies, *J. Comput. Assist. Tomogr.*, **14**, 163–164.
- Tofts, P. S., Wicks, D. A. and Barker, G. J. 1991a, The MRI measurement of NMR and physiological parameters in tissue to study disease process, *Prog. Clin. Biol. Res.*, **363**, 313–325.
- Tofts, P. S., Wicks, D. A. G. and Barker, G. J. 1991b, The MRI measurement of NMR and physiological parameters in tissue to study disease process., in *Information Processing in Medical Imaging*, Ortendahl, D. A. and Llacer J., (eds.), Wiley-Liss, New York, 313–325.
- Tofts, P. S., Barker, G. J., Simmons, A., MacManus, D. G., Thorpe, J., Gass, A. and Miller, D. H. 1994, Correction of nonuniformity in images of the spine and optic nerve from fixed receive-only surface coils at 1.5 T, *J. Comput. Assist. Tomogr.*, **18**, 997–1003.
- Topp, S., Adalsteinsson, E. and Spielman, D. 1997, Fast multislice  $B_1$ -mapping, *Proc. Int. Soc. Magn. Reson. Med.*, **5**, 281.
- Tropp, J. 1993, An extended reciprocity principle for NMR reception, *Proc. Int. Soc. Magn. Reson. Med.*, 1320.
- Tubridy, N. and McKinstry, C. S. 2000, Neuroradiological history: Sir Joseph Larmor and the basis of MRI physics, *Neuroradiology*, **42**, 852–855.
- van Waesberghe, J. H., Castelijns, J. A., Scheltens, P., Truyen, L., Lycklana, A. N. G., Hoogenraad, F. G., Polman, C. H., Valk, J. and Barkhof, F. 1997, Comparison of four potential MR parameters for severe tissue destruction in multiple sclerosis lesions, *Magn. Reson. Imag.*, **15**, 155–162.
- Vaughan, J. T., Garwood, M., Collins, C. M., Liu, W., DelaBarre, L., Adriany, G., Andersen, P., Merkle, H., Goebel, R., Smith, M. B. and Ugurbil, K. 2001, 7 T vs. 4 T: RF power, homogeneity, and signal-to-noise

- comparison in head images, *Magn. Reson. Med.*, **46**, 24–30.
- Venkatesan, R., Lin, W. and Haacke, E. M. 1998, Accurate determination of spin-density and  $T_1$  in the presence of RF-field inhomogeneities and flip-angle miscalibration, *Magn. Reson. Med.*, **40**, 592–602.
- Wheeler-Kingshott, C. A., Parker, G. J., Symms, M. R., Hickman, S. J., Tofts, P. S., Miller, D. H. and Barker, G. J. 2002, ADC mapping of the human optic nerve: increased resolution, coverage, and reliability with CSF-suppressed ZOOM-EPI, *Magn. Reson. Med.*, **47**, 24–31.
- Whittall, K. P., MacKay, A. L., Graeb, D. A., Nugent, R. A., Li, D. K. and Paty, D. W. 1997, In vivo measurement of  $T_2$  distributions and water contents in normal human brain, *Magn. Reson. Med.*, **37**, 34–43.
- Wicks, D. A., Barker, G. J. and Tofts, P. S. 1993, Correction of intensity nonuniformity in MR images of any orientation, *Magn. Reson. Imag.*, **11**, 183–196.
- Willcott, M. R., III, Mee, G. L. and Chesick, J. P. 1987, Magnetic field mapping in NMR imaging, *Magn. Reson. Imag.*, **5**, 301–306.
- Young, I. R. and Payne, J. A. 1987, Slice-shape artifact changes with precession angle in rapid MR imaging, *Magn. Reson. Med.*, **5**, 177–181.
- Zelaya, F. O., Roffmann, W. U., Crozier, S., Teed, S., Gross, D. and Doddrell, D. M. 1997, Direct visualisation of  $B_1$  inhomogeneity by flip angle dependency, *Magn. Reson. Imag.*, **15**, 497–504.
- Zweig, M. H. and Campbell, G. 1993, Receiver-operating characteristic (ROC) plots: a fundamental evaluation tool in clinical medicine, *Clin. Chem.*, **39**, 561–577.

**Queries in Chapter 2:**

- Q1. There is citation for table 2.5 but there is no table, kindly provide us.
- Q2. Parkes *et al*, 2003, submitted–update?